Research Square

Preprints are preliminary reports that have not undergone peer review.
They should not be considered conclusive, used to inform clinical practice,
or referenced by the media as validated information.

Spatial Multi-Omics Reveals an Immunometabolic Niche Defined by PROM1+SLC27A4+ Tumor-Initiating Cells and CD8A+ABCA12+ Exhausted T Cells in HER2-Positive Breast Cancer

Huijing Yin

yinhuijing_001@163.com

Institute for Clinical Research

Huijing Yin

Institute for Clinical Research

Wei Wang

Shanghai General Hospital

Xingning Fu

Ling Hong

Dawen Zheng

Hongyan Liu

Wei Jin

Shanghai Jiao Tong University School of Medicine

Yicheng Lv

Ye Sun

Zhikang Zhang

Xiufeng Yang

Guiyan Han

Zheng Li

Xiaoying Tan

Yunting Li

Tianlong Gao

Wei Li

Wenhua Liang

Xiaotong Dong

Li Zhu

Yunxiang Zhang

Article

Keywords: CD8A+ABCA12+ T cells, T cell exhaustion, HER2-positive breast cancer, Tumor-initiating cells, Lipid metabolism, Peri-droplet mitochondria, Spatial multi-omics

Posted Date: September 14th, 2026

DOI: https://doi.org/10.21203/rs.3.rs-10887996/v1

License: This work is licensed under a Creative Commons Attribution 4.0 International License.
Read Full License

Additional Declarations: There is **NO** conflict of interest to disclose.

Spatial Multi-Omics Reveals an Immunometabolic Niche Defined by PROM1^{+}SLC27A4^{+} Tumor-Initiating Cells and CD8A^{+}ABCA12^{+} Exhausted T Cells in HER2-Positive Breast Cancer

Huijing Yin[1,14,15*], Wei Wang[2,14], Xingning Fu[3,14], Ling Hong[4,14], Dawen Zheng[2,14], Hongyan Liu[5,14], Wei Jin [6,14,] , Yicheng Lv[1,14], Ye Sun[7,14], Zhikang Zhang[5], Xiufeng Yang[5], Guiyan Han[3], Zheng Li[8], Xiaoying Tan[3], Yunting Li[3], Tianlong Gao[9], Wei Li[10,11], Wenhua Liang[12], Xiaotong Dong[3], Li Zhu[2*], Yunxiang Zhang[3*]

1. Precision Research Center for Refractory Diseases, Institute for Clinical Research, Shanghai General Hospital, Shanghai Jiao Tong University School of Medicine, Shanghai, China.
2. Department of General Surgery, Shanghai General Hospital, Shanghai Jiao Tong University School of Medicine, Shanghai, China.
3. Center of Precision Pathologic Diagnosis, Weifang People's Hospital, Weifang, Shandong, China.
4. Shanghai First Maternity and Infant Hospital, Tongji University School of Medicine, Shanghai, China.
5. OE Biotech Co., Ltd., Shanghai, China.
6. Shanghai Institute of Immunology, Department of Immunology and Microbiology, Shanghai Jiao Tong University School of Medicine, Shanghai, China.
7. Carl Zeiss (Shanghai) Co., Ltd., Shanghai, China.
8. Weiya Electron Microscopy, Jinan, Shandong, China.
9. Leica Microsystems (Shanghai) Co. Ltd., Shanghai, China.
10. Advanced Innovation Center for Human Brain Protection, National Clinical Research Center for Geriatric Disorders, Xuanwu Hospital Capital Medical University, Beijing, China.
11. Aging Translational Medicine Center, International Center for Aging and Cancer, Beijing Municipal Geriatric Medical Research Center, Xuanwu Hospital, Capital Medical University, Beijing, China.
12. Department of Immunology and Microbiology, State Key Laboratory of Oncogenes and Related Genes, Shanghai Jiao Tong University School of Medicine, Shanghai, China.
14. These authors contributed equally to this work.
15. Lead Contact.

* Correspondence:
Huijing Yin (Lead Contact), yinhuijing_001@163.com. Address: NO.650, Xinsongjiang Road, Shanghai, China.
Li Zhu, zhuli8@yeah.net. Address: No. 85, Wujin Road, Hongkou District, Shanghai, China
Yunxiang Zhang, zhangyunxiang@uhrs.edu.cn. Address: NO.151, Guangwen Street, Weifang, China.

Abstract

Despite targeted therapy advances, drug resistance and metastasis remain the primary causes of mortality in HER2-positive breast cancer. The crosstalk between tumor-initiating cells (TICs) and specific $CD8^+$ T cell subsets in the tumor microenvironment (TME) that may contribute to treatment failure remains poorly defined. Here, by integrating snRNA-seq (N=20), spatial transcriptomics with spatial metabolomics (N=5), spatial in situ analysis (N=42), proteomics (N=12), functional co-culture assays, and clinical tissue validation (N=279), as well as reanalysis of public datasets (N=35), we identified a $PROM1^+SLC27A4^+$ TICs (tumor-initiating cells) – associated $CD8A^+ABCA12^+$ exhausted T cell population enriched in HER2-positive breast cancer. Spatial and functional analyses support a model in which $PROM1^+SLC27A4^+$ TICs engage EGFR-expressing $CD8A^+ABCA12^+$ cells through an EGF-enriched signaling axis, consistent with STAT5-dependent upregulation of TIGIT and ABCA12. In turn, $CD8A^+ABCA12^+$ cells facilitate ABCA12-dependent lignoceric acid release, putatively imported by $PROM1^+SLC27A4^+$ TICs in a SLC27A4-dependent manner, associated with peri-droplet mitochondrial (PDM) remodeling, MFN2 upregulation and enhanced ATP production. Trajectory analyses suggest that $CD8A^+ABCA12^+$ cells are transcriptionally and spatially connected to $CD8A^+ITGAE^+$ tissue-resident memory cells, consistent with a putative exhaustion-associated state transition. $CD8A^+ABCA12^+$ cells were enriched in primary tumors, metastatic lesions and post-chemotherapy specimens, correlating with poor clinical outcome. These findings define an immunometabolic TIC-associated niche that may contribute to therapy resistance and metastatic progression in HER2-positive breast cancer.

Keywords: $CD8A^+ABCA12^+$ T cells, T cell exhaustion, HER2-positive breast cancer, Tumor-initiating cells，Lipid metabolism，Peri-droplet mitochondria, Spatial multi-omics

1. Introduction

Treatment failure in HER2-positive breast cancer—affecting ~20% of all breast cancer patients—is driven not only by cell-autonomous alterations (HER2 amplification, PI3K-AKT-mTOR mutations, PTEN loss) but increasingly by reciprocal co-evolution between cancer cells and the tumor microenvironment (TME) [1-4]. Despite significant advances from anti-HER2 therapies (trastuzumab, pertuzumab, ado-trastuzumab emtansine),30-50% of patients develop acquired resistance and up to 60% experience distant metastasis [3-4], and the 5-year mortality exceeds 40% in metastatic cases [5]. These statistics underscore an urgent need to decode TME-dependent resistance mechanisms beyond cancer cell-intrinsic pathways.

A critical yet underexplored node in this co-evolution is the tumor-initiating cell (TIC)-immune cell axis. TICs, defined by self-renewal capacity and metastatic potential, have been linked to resistance and relapse across multiple cancer types [6,7]. Among TIC-associated molecules, PROM1 (CD133) regulates self-renewal and metastatic potential [8-9]. Our study identifies a previously underappreciated PROM1$^+$SLC27A4$^+$ double-positive TIC subpopulation that actively constructs specialized ecological niches to sustain survival, drive recurrence, and enhance metastatic capacity. However, the immune cell partners and molecular mechanisms mediating this niche construction in HER2-positive breast cancer remain entirely unknown—representing the central gap this study addresses.

On the immune side, CD8$^+$ T cell exhaustion is well-recognized in tumor immunity, yet the exhaustion landscape is deeply heterogeneous: distinct subsets such as CD8$^+$GZMB$^+$ and pre-exhausted CD8$^+$GZMK$^+$ populations differentially dictate immunotherapy outcomes [10], and immune checkpoint blockade shows suboptimal efficacy in breast cancer, with certain CD8$^+$ subsets further depleted following treatment [11]. Whether TICs specifically co-opt a defined exhausted CD8$^+$ T cell subset to construct a drug tolerance- and metastasis-associated niche, rather than inducing generalized CD8$^+$ exhaustion, has not been systematically examined in HER2-positive breast cancer. Furthermore, tissue-resident memory T cells (TRMs), key regulators of local immune surveillance, may serve as the precursor pool for such TIC-reprogrammed subsets, yet this lineage relationship remains entirely uncharacterized.

Resolving these gaps requires not only identifying the specific immune partners of PROM1$^+$SLC27A4$^+$ TICs, but also decoding the reciprocal metabolic crosstalk that sustains the ecological niche—specifically, how lipid metabolites may shuttle between TICs and exhausted T cell subsets to fuel drug tolerance and metastatic energy demands. Traditional bulk omics approaches average signals across heterogeneous populations and cannot capture the spatial proximity that directly dictates TIC-immune functional crosstalk [12]; integrated spatial multi-omics is therefore essential to resolve these dynamics within their native TME context [13].

To address these questions, we combined spatial transcriptomics, metabolomics, spatial in situ analysis, and proteomics with functional assays, and clinicopathological analysis. We identify CD8A$^+$ABCA12$^+$ cells as a previously underappreciated exhausted T cell subset reprogrammed by PROM1$^+$SLC27A4$^+$ TICs via the EGF-EGFR-STAT5-TIGIT/ABCA12 signaling cascade, characterize a putative differentiation trajectory from TRM-CD8A$^+$ITGAE$^+$ cells, and demonstrate that ABCA12-dependent fatty acid efflux from

CD8A$^+$ABCA12$^+$ cells is associated with SLC27A4-mediated lipid uptake, peri-droplet mitochondrial (PDM) remodeling, and enhanced ATP production in TLCs to power drug resistance and metastasis. Collectively, these findings support the hypothesis that the PROM1+SLC27A4+ - CD8A+ABCA12+ immunometabolic axis constitutes a treatment resistance- and metastasis-associated ecological niche, and provide a compelling rationale for targeting this axis in HER2-positive breast cancer.

2. Results

2.1 Single-nucleus RNA sequencing (snRNA-seq) identified previously underappreciated exhausted T cell subpopulations in HER2-positive breast cancer

To investigate the phenotypic characteristics and temporal dynamics of intratumoral T cells, we performed single-nucleus RNA sequencing (snRNA-seq) on tumor samples collected from 20 patients with HER2-positive breast cancer. After applying stringent quality control criteria, a total of 11,570 high-quality nuclei were included in the downstream analyses.

Unsupervised clustering combined with t-distributed stochastic neighbor embedding (tSNE) visualization identified nine distinct subpopulations among T cells and natural killer (NK) cells (**Fig. 1A**). CD4$^+$ T cells were delineated by the expression of CD3E, CD3D, and CD4, while CD8$^+$ T cells were defined by CD3E, CD3D, CD8A, and CD8B expression. NK cells were distinguished by the absence of CD3 expression and positive expression of NKG7. The identified subpopulations included CD4$^+$ T cells (C03_TOX2, C05_ST8SIA1 and C06_TCF7), CD8$^+$ T cells (C01_ITGAE, C02_ABCA12, C04_KLRF1, C07_SLC24A3 and C09_BCL11A), and NK cells (C08_KLRC1). For in-depth investigation of T cell putative differentiation and exhaustion, the C01_ITGAE and C02_ABCA12 subpopulations were specifically isolated. Pseudo-time trajectory analysis suggested a putative transcriptional state transition, with C01_ITGAE occupying an earlier pseudotime position relative to C02_ABCA12 (**Fig. 1B** and **1C**).

We further characterized these two subpopulations using a panel of markers associated with canonical T cell characteristics (**Fig. 1D**). Both C01_ITGAE and C02_ABCA12 subpopulations exhibited upregulated expression of tissue-resident memory (TRM) cell markers and exhaustion-related molecules. Compared with C02_ABCA12 cells, C01_ITGAE cells displayed higher expression of markers associated with stemness and effector function-associated markers. A previous study proposed a four-stage exhaustion progression model based on SLAMF6 and CD69 expression, comprising SLAMF6$^+$CD69$^+$, SLAMF6$^+$CD69$^-$, SLAMF6$^-$CD69$^-$, and SLAMF6$^-$CD69$^+$ states (**Fig. 1E**) [14]. Consistent with this model, we observed distinct expression patterns of SLAMF6 and CD69 across the two subpopulations (**Fig. 1F**). Pie chart-based analysis of exhaustion stage distribution further supported a sequential exhaustion trajectory from C01_ITGAE to C02_ABCA12 cells (**Fig. 1G**).

While SLAMF6 and CD69 were used here to align our data with a previously reported exhaustion progression framework, we next sought to identify a marker that could further resolve more dysfunction-associated state within the CD8A$^+$ABCA12$^+$ population and could be robustly applied in tissue-based spatial analyses. Among the exhaustion-associated molecules shown in Fig. 1D, TIGIT was one of the most prominently

upregulated markers in C02_ABCA12 cells. Given previous reports linking TIGIT expression to a more advanced dysfunctional/exhausted T-cell state [15-17], we used TIGIT as an additional marker to stratify the CD8A$^+$ABCA12$^+$ compartment into subpopulations with relatively lower versus higher more dysfunction-associated state.

To further dissect the spatial distribution of these exhausted T cell subsets in HER2-positive invasive breast cancer tissues, multiplex immunofluorescence staining was employed to detect the localization and expression of CD8A, ABCA12, and TIGIT. Accordingly, CD8A$^+$ABCA12$^+$TIGIT$^-$ cells were classified as a relatively less exhausted subset and CD8A$^+$ABCA12$^+$TIGIT$^+$ cells were classified as a relatively more exhausted subset for spatial analysis.

Based on the nearest CD8A$^+$ABCA12$^+$TIGIT$^+$ cell to each CD8A$^+$ABCA12$^+$TIGIT$^-$ cell (**Fig. 1H)**, eight representative pathological regions were identified for further analysis (**Fig. 1I**). The spatial distance between CD8A$^+$ABCA12$^+$TIGIT$^-$ cells and CD8A$^+$ABCA12$^+$TIGIT$^+$ cells was quantified using the Detect Centroid Distances 2D function in the Spatial Analysis module of QuPath (**Fig. 1J**). In this analysis, red points indicate CD8A$^+$ABCA12$^+$TIGIT$^-$ cells located in close proximity to CD8A$^+$ABCA12$^+$TIGIT$^+$ cells, whereas blue points indicate greater distance between the two cell populations. Our results revealed that regions with a dense exhaustion gradient were distributed mainly in two pathological contexts: 1) tumor regions with extensive lymphocytic infiltration; and 2) necrotic regions, particularly intraductal necrosis and intraluminal necrosis.

To assess whether the identified CD8A$^+$ABCA12$^+$ T cell population could be detected in an independent and larger sample set, we reanalyzed publicly available scRNA-seq datasets comprising 35 patients [6,9]. At single-cell resolution, the corresponding CD8A$^+$ABCA12$^+$ T cell population were identified, and their relative abundances were quantified across individual patient samples. We then examined the associations between the proportions of these cells and available clinical characteristics. In this cohort, the total number of lymphocytes per patient ranged from 153 to 5,117, with a mean of 1,728 cells, providing a quantitative basis for estimating the frequency of the target CD8A$^+$ABCA12$^+$ T cell population.

Clinically, group-wise comparisons showed that CD8A$^+$ABCA12$^+$ T cells were enriched in HER2-positive tumors (**Fig. 1K**) and more aggressive molecular subtypes (**Fig. 1L**). Their proportion was also higher in tumors with advanced histological grades (**Fig. 1M**). Among the 35 patients, prognostic follow-up information was available for 21 individuals, who were therefore included in the survival analysis. Patients with a higher abundance of CD8A$^+$ABCA12$^+$ T cells showed significantly shorter overall survival (**Fig. 1N**) and progression-free survival (**Fig. 1O**). Given the limited number of patients with follow-up data, this survival analysis should be interpreted as exploratory.

These results not only highlight the need for further investigation into the characteristics and functions of the previously underappreciated CD8A$^+$ABCA12$^+$ T cell subpopulation but also underscore the importance of exploring its potential crosstalk with cancer cells.

2.2 In-depth characterization of the previously uncharacterized exhausted CD8A$^+$ABCA12$^+$ T cell subset

Next, we aimed to clarify the characteristic features of the CD8A$^+$ABCA12$^+$ subpopulation, particularly its role in T cell exhaustion. Violin plots revealed a significant upregulation of exhaustion-related genes in CD8A$^+$ABCA12$^+$ cells compared with CD8A$^+$ABCA12$^-$ cells (**Fig. 2A**). To validate these findings at the protein level, we prepared single-cell suspensions from breast cancer surgical specimens and performed flow cytometry analysis (**Fig. 2B**). Compared with CD8A$^+$ABCA12$^-$cells, CD8A$^+$ABCA12$^+$ cells showed a marked upregulation of both T cell exhaustion markers and tissue-resident memory (TRM) markers. In contrast, they exhibited reduced expression of markers associated with T cell stemness, activation, proliferation, and effector function (**Fig. 2C**). These results suggest that the CD8A$^+$ABCA12$^+$ subpopulation represents an exhausted TRM-like T cell subset with distinct phenotypic features. Notably, while CD8A$^+$ABCA12$^+$ cells retain partial TRM-associated marker expression (including residual ITGAE), their overall transcriptional and phenotypic profile is distinct from the CD8A$^+$ITGAE$^+$ population, consistent with a model of progressive state transition rather than discrete binary differentiation. The persistence of certain TRM markers in CD8A$^+$ABCA12$^+$ cells may reflect an intermediate or hybrid exhaustion-TRM state, as has been described in other tumor contexts

2.3 Tumor-initiating PROM1$^+$SLC27A4$^+$ cells engage in crosstalk with CD8A$^+$ABCA12$^+$ T cells through the EGF-EGFR ligand-receptor axis

To explore the association between CD8A$^+$ABCA12$^+$ T cells and cancer cells, we first divided epithelial cells into 11 distinct subpopulations (**SFig. 1A**). We then analyzed the outgoing (**SFig. 1B**) and incoming (**SFig. 1C**) cell communication networks between these 11 epithelial subpopulations and CD8A$^+$ABCA12$^+$ T cells. These analyses revealed extensive communication between CD8A$^+$ABCA12$^+$ T cells and several epithelial subpopulations. Our preliminary results indicated that the PROM1$^+$SLC27A4$^+$ epithelial subpopulation within Epithelial_C10_SLC27A4 accounted for the highest proportion among all epithelial subpopulations (**SFig. 1D**). Three-dimensional (3D) spheroid assays confirmed that PROM1$^+$SLC27A4$^+$ epithelial cells possessed stem-like spheroid-forming capabilities. Moreover, co-culture experiments further revealed that CD8A$^+$ABCA12$^+$ T cells enhanced the stemness of PROM1$^+$SLC27A4$^+$ epithelial cells (**SFig. 1E-G**).

Clinical subgroup comparisons showed that PROM1$^+$SLC27A4$^+$ cells were more abundant in HER2-positive tumors than in other molecular subtypes (**Fig. 3A**). Compared with peripheral blood mononuclear cells (PBMCs) and adjacent non-tumor tissues, PROM1$^+$SLC27A4$^+$ cells were preferentially enriched in tumor tissues (**Fig. 3B**). Higher proportions of PROM1$^+$SLC27A4$^+$ cells were also observed in breast cancer patients with lymph node metastasis or distant lung metastasis (**Fig. 3C-D**).

Furthermore, dot plot analysis revealed a unique expression pattern of the EGF-EGFR ligand-receptor pair, in which the PROM1$^+$SLC27A4$^+$ subpopulation served as the ligand-secreting cells and the CD8A$^+$ABCA12$^+$ subpopulation acted as the receptor-expressing cells (**Fig. 3E**). By comparing CD8A$^+$ABCA12$^+$ T cells cultured alone and co-cultured with PROM1$^+$SLC27A4$^+$ cells, SCENIC analysis supported that inferred STAT5 regulon activity was higher in the co-culture group than in the monoculture group (**Fig. 3F-G**), suggesting that PROM1$^+$SLC27A4$^+$ cells contribute to the activation of STAT5 signaling in

CD8A$^+$ABCA12$^+$ T cells. Integrated regulatory network analysis highlighted TIGIT and ABCA12 (marked with stars) as putative STAT5-associated target genes (**Fig. 3H**). Next, to explore whether EGFR is associated with STAT5, we sorted PROM1$^+$SLC27A4$^+$ and CD8A$^+$ABCA12$^+$ subpopulations from breast cancer tissues. We found that co-culture of CD8A$^+$ABCA12$^+$ cells with PROM1$^+$SLC27A4$^+$ cells increased the phosphorylation of EGFR and STAT5 compared with CD8A$^+$ABCA12$^+$ monoculture. Treatment with the EGFR inhibitor erlotinib suppressed the activation of both phosphorylated EGFR (p-EGFR) and phosphorylated STAT5 (p-STAT5) (**Fig. 3I**). Subsequent *STAT5* knockdown experiments resulted in reduced expression of TIGIT and ABCA12 at both transcriptional and protein levels in the co-culture system (**Fig. 3J-K**), indicating that the EGFR-STAT5 axis exerts a dual regulatory effect on TIGIT and ABCA12. Collectively, these results support a model in which PROM1$^+$SLC27A4$^+$ cells signal to EGFR-expressing CD8A$^+$ABCA12$^+$ T cells via EGF, activating the EGFR-STAT5 axis to upregulate TIGIT and ABCA12 expression.

2.4 Spatial transcriptomic profiling of CD8A$^+$ABCA12$^+$ T cell exhaustion trajectories using stLearn trajectory and neighbor analyses

Building on previous findings that C02_ABCA12 cells may represent the downstream differentiated subset of C01_ITGAE cells (Fig. 1B-C), and that C02_ABCA12 cells possess TRM characteristics (Fig. 1D and 2C), we employed spatial transcriptomics to dissect the spatial trajectory of putative differentiation from CD8A$^+$ITGAE$^+$ to CD8A$^+$ABCA12$^+$ cells, as well as the exhaustion dynamics accompanying this differentiation process.

Tissue specimens were obtained from five individuals diagnosed with HER2 overexpressing breast cancer. Across these five samples, we analyzed the spatial positional information of three key cell subpopulations: PROM1$^+$SLC27A4$^+$, CD8A$^+$ITGAE$^+$, and CD8A$^+$ABCA12$^+$ cells (**Fig. 4A**). Local differentiation trajectories were constructed using stLearn-based computational analysis, with spatial trajectory distances quantified between CD8A$^+$ITGAE$^+$ cells (designated as state 0, corresponding to the early differentiation phase) and CD8A$^+$ABCA12$^+$ cells (designated as state 1, representing the late differentiation phase) **(Fig. 4B-F**). Differentiation tree models were established to visualize the transition routes from CD8A$^+$ITGAE$^+$ cells (mapped to the indigo-colored spatial region) to CD8A$^+$ABCA12$^+$ cells (mapped to the ginger yellow spatial area) (**Fig. 4G-K**). Transition genes—characterized as genes showing consistent monotonic expression alterations throughout the differentiation process from CD8A$^+$ITGAE$^+$ to CD8A$^+$ABCA12$^+$ cells—were screened and identified (**Fig. 4L**). Among the genes upregulated along this differentiation trajectory (marked in cherry pink), *TIGIT* was recurrently identified among the upregulated transition genes. This observation suggests that *TIGIT* upregulation is associated with the progression of T cell exhaustion along this differentiation trajectory in HER2$^+$ breast cancer patients, underscoring its potential utility as a candidate indicator for assessing the degree of T cell exhaustion.

Spatial neighbor analysis based on Euclidean distance metrics (**Fig. 4M-Q**) revealed that both CD8A$^+$ITGAE$^+$ and CD8A$^+$ABCA12$^+$ subpopulations—especially CD8A$^+$ABCA12$^+$ cells—localized in close proximity to PROM1$^+$SLC27A4$^+$ cells across all samples. Furthermore, a Cottrazm-based pathological annotation approach was used to jointly define the malignant-boundary-nonmalignant spatial axis (**Fig. 4R**). Mountain plot

comparisons showed that, compared with the PROM1$^+$SLC27A4$^-$ subpopulation, the PROM1$^+$SLC27A4$^+$ subpopulation was significantly upregulated in the malignant tumor microenvironment (**Fig. 4S**). In contrast, the CD8A$^+$ABCA12$^+$ subpopulation—relative to CD8A$^+$ABCA12$^-$ cells—was upregulated both at the malignant-nonmalignant tumor boundary and within the malignant tumor microenvironment (**Fig. 4T**). Collectively, these spatial distribution patterns indicate that CD8A$^+$ABCA12$^+$ cells are preferentially co-localized with PROM1$^+$SLC27A4$^+$ tumor cells within the malignant tumor microenvironment, suggesting a close spatial association between exhausted T cells and tumor cells. This co-localization pattern is consistent with the possibility that sustained proximity to PROM1$^+$SLC27A4$^+$ tumor cells may contribute to T cell functional reprogramming and the progressive loss of anti-tumor immune capacity in HER2-positive breast cancer.

2.5 Integrated spatial metabolomic and transcriptomic profiling reveals lignoceric acid-centered spatial gradients between PROM1$^+$SLC27A4$^+$ and CD8A$^+$ABCA12$^+$ enriched regions

Given that our aforementioned results indicated PROM1$^+$SLC27A4$^+$ cells interact with CD8A$^+$ABCA12$^+$ cells via EGF, and that ABCA12 has been implicated in ceramide / fatty acid transport [18-19], we sought to investigate the spatial distribution of related metabolites and signaling pathway activity in regions enriched for these two subpopulations.

First, we established an integrated analytical approach combining spatial transcriptomics and spatial metabolomics, and performed spatial metabolomic analysis on the aforementioned spatial transcriptomic samples. The analytical framework integrated spatial metabolomics and transcriptomics, adopting a randomized six-point linear sampling strategy across five tissue sections (**Fig. 5A I-V**). Initially, tissue sections were radially divided into 16 concentric zones starting from the central origin, with spatial mapping conducted for each zone (**Fig. 5B I-V**). Subsequently, SSCC clustering identified spots with high CD8A$^+$ABCA12$^+$-like and PROM1$^+$SLC27A4$^+$-like signature scores, enabling visualization of their spatial distribution patterns (**Fig. 5C I-V**). Following this, spatial gradients of EGFR pathway activity were reconstructed across the radial zones (**Fig. 5D I-V**). Finally, spatial distribution maps of lignoceric acid and ceramide-associated metabolites were generated according to intensity gradients across the radial zones (**Fig. 5E I-V**). We integrated spatial transcriptomic EGFR pathway activity with spatial lipidomic features, including fatty acid-and ceramide-associated metabolites. The preferential spatial enrichment of lignoceric acid in CD8A$^+$ABCA12$^+$- and PROM1$^+$SLC27A4$^+$-enriched regions is consistent with, but does not by itself establish, an ABCA12-mediated transfer mechanism. The functional evidence for this transfer is provided by the pulse-chase experiments described in Section 2.6, where spatial metabolomics data serve as in situ corroborative evidence for the regional specificity of this metabolic exchange.

2.6 CD8A$^+$ABCA12$^+$ T cells promote peridroplet mitochondrial remodeling in PROM1$^+$SLC27A4$^+$ tumor cells via ABCA12-dependent lignoceric acid transfer

Next, we investigated how CD8A$^+$ABCA12$^+$ T cells functionally regulate PROM1$^+$SLC27A4$^+$ tumor cells. Based on GSVA enrichment scores of PROM1$^+$SLC27A4$^+$ cells cultured alone and those co-cultured with CD8A$^+$ABCA12$^+$ cells, the top enriched GO

terms in co-cultured PROM1$^+$SLC27A4$^+$ cells included "Fatty acid transmembrane transport", "Fatty acid derivative metabolic process", and "Mitochondrial fusion" (**SFig. 2A**). For KEGG pathways, enrichment was concentrated in metabolic pathways, particularly "Fatty acid metabolism" (**SFig. 2B**). To identify key genes potentially involved in fatty acid transmembrane transport and mitochondrial fusion, we performed comparative analysis across three groups: PROM1$^+$SLC27A4$^+$ cells alone, PROM1$^+$SLC27A4$^+$ cells co-cultured with CD8A$^+$ABCA12$^+$ cells, and PROM1$^+$SLC27A4$^+$ cells co-cultured with CD8A$^+$ABCA12$^-$ cells. Genes selectively upregulated in PROM1$^+$SLC27A4$^+$ cells co-cultured with CD8A$^+$ABCA12$^+$ T cells, but not in the other two groups, were prioritized. Heatmap analysis identified SLC27A4 and MFN2 as candidate genes selectively upregulated under CD8A$^+$ABCA12$^+$ T cell co-culture conditions (**SFig. 2C**). Finally, co-expression network module analysis was conducted to delineate key biological function hubs among the enriched genes, further linking SLC27A4 and MFN2 to fatty acid transmembrane transport and mitochondrial fusion, respectively.

Based on these bioinformatics clues, we proposed the hypothesis that CD8A$^+$ABCA12$^+$ cells may promote mitochondrial remodeling in PROM1$^+$SLC27A4$^+$ cells via fatty acid transport. To verify this hypothesis, we designed the following experiments (**Fig. 6A**): lignoceric acid in CD8A$^+$ABCA12$^+$ cells were fluorescently labeled, and a Pulse-Chase assay was performed. Co-culture with PROM1$^+$SLC27A4$^+$ cells was conducted, and the presence of fluorescent lipid-containing particles in the supernatant was used to evaluate whether fatty acids were transported across the membrane from CD8A$^+$ABCA12$^+$ cells. Mitochondria in PROM1$^+$SLC27A4$^+$ cells were labeled with a fluorescent tracer to assess the localization of fatty acids transported from CD8A$^+$ABCA12$^+$ cells within PROM1$^+$SLC27A4$^+$ mitochondria. A follow-up experimental design was implemented (**Fig. 6B**): CD8A$^+$ABCA12$^+$ cells were treated with si-*ABCA12*, or *SLC27A4* was knocked down in PROM1$^+$SLC27A4$^+$ cells, to evaluate the impact on fatty acid transport between the two subpopulations. The results showed (**Fig. 6C**) that *ABCA12* knockdown led to a significant reduction in fluorescent lipid-containing signals in the supernatant, indicating impaired lignoceric acid export from CD8A$^+$ABCA12$^+$ cells. *SLC27A4* knockdown resulted in minimal localization of lipid droplets in PROM1$^+$SLC27A4$^+$ mitochondria, despite the presence of lipid-containing signals in the supernatant, suggesting blocked lignoceric acid uptake by PROM1$^+$SLC27A4$^+$ cells. These findings indicate the critical roles of *ABCA12* and *SLC27A4* in lignoceric acid transport between the two subpopulations.

PDMs were operationally defined as mitochondria in direct physical contact with or spatially adjacent to lipid droplets, based on established ultrastructural criteria. Further transmission electron microscopy (TEM) analysis (**Fig. 6D**) revealed that lipid droplets resided around mitochondria, forming PDM structures, and some mitochondria underwent fusion. Supporting a model, in the co-culture system, treatment of CD8A$^+$ABCA12$^+$ cells with the si-*ABCA12* suppressed the expression of the mitochondrial fusion gene MFN2 (**Fig. 6E**), indicating that fatty acids transported by *ABCA12* in CD8A$^+$ABCA12$^+$ cells are crucial for mitochondrial fusion. Additionally, *MFN2* knockdown in the co-culture system not only inhibited mitochondrial fusion (**Fig. 6F**) but also reduced lipid droplet–mitochondria contacts and PDM-like structures (**Fig. 6G**). This suggests a potential logical sequence: these findings support a model in which ABCA12-dependent lignoceric acid transfer is

coupled to MFN2-associated mitochondrial remodeling and PDM formation in PROM1$^+$SLC27A4$^+$ cells, facilitating lipid droplet–mitochondria coupling and the delivery of lipid-derived substrates for mitochondrial oxidation for key biological processes. Fluorescent labeling of live cells confirmed that a large number of increased physical coupling between lipid droplets and mitochondria, consistent with enhanced lipid utilization through mitochondrial fatty acid oxidation (**Fig. 6H**). These lipid droplets are primarily used for fatty acid oxidation to generate substantial ATP. Compared with PROM1$^+$SLC27A4$^+$ cells cultured alone, co-culture with CD8A$^+$ABCA12$^+$ cells significantly increased the ATP synthesis rate (**Fig. 6I**). This increase was attenuated by *ABCA12* knockdown in CD8A$^+$ABCA12$^+$ cells or SLC27A4 knockdown in PROM1$^+$SLC27A4$^+$ cells (**Fig. 6I**), supporting the functional dependence of enhanced ATP production on ABCA12-mediated lignoceric acid transfer and SLC27A4-dependent uptake. As illustrated in the schematic diagram (**Fig. 6J**), mitochondria can increase the surface area of the inner mitochondrial membrane through membrane fusion, thereby expanding the site for oxidative phosphorylation reactions [20-22], which accelerates ATP generation.

We employed subcellular 3D reconstruction based on TEM imaging to further quantify organelle remodeling (**Fig. 6K**). For PROM1$^+$SLC27A4$^+$ cells cultured alone and those co-cultured with CD8A$^+$ABCA12$^+$ cells, 2D and 3D structural images of mitochondria were acquired (**Fig. 6L**), along with 3D panoramic and zoomed-in images showing the spatial relationship between mitochondria and lipid droplets (**Fig. 6M**). Quantitative analysis revealed significant differences between the two groups in mitochondrial parameters, including mitochondrial sphericity, mitochondrial volume, mitochondria-to-nucleus distance, and mitochondria-to-lipid droplet distance (**Fig. 6N**). Differences were also observed in lipid droplet parameters, such as lipid droplet sphericity, lipid droplet volume, lipid droplet-to-nucleus distance, and lipid droplet-to-mitochondria distance (**Fig. 6O**). These results indicate that not only can PROM1$^+$SLC27A4$^+$ cells induce exhaustion of CD8A$^+$ABCA12$^+$ cells, but exhausted CD8A$^+$ABCA12$^+$ cells can further support PROM1$^+$SLC27A4$^+$ cells—providing lignoceric acid materials for energy synthesis while driving organelle-level modifications in PROM1$^+$SLC27A4$^+$ cells to adapt to changes brought about by co-evolution.

2.7 Spatial distribution characteristics of CD8A$^+$ABCA12$^+$ and PROM1$^+$SLC27A4$^+$ subsets in breast cancer patients with lung or lymph node metastasis

Building on previous analyses that revealed expression differences of the PROM1$^+$SLC27A4$^+$ subpopulation between lymph node and lung metastases (Fig. 3C-D), we employed multiplex immunohistochemistry combined with a four-part analytical pipeline for comprehensive spatiotemporal profiling. This pipeline utilized Phenochart for ROI segmentation, inForm for spectral deconvolution and cell phenotyping, QuPath for generating distance heatmaps and merging images, and the phenoptrReports package for cell-to-cell distance calculations.

Within the lung metastasis sites, we identified 5 key regions based on the distribution patterns and association strength of CD8A$^+$ABCA12$^+$ and PROM1$^+$SLC27A4$^+$ cell subpopulations (**Fig. 7A-B**). Spatial distance analyses, visualized through panoramic heatmaps (**Fig. 7C**), revealed that the two subpopulations were in closer proximity in the

lung bronchus (ROI1) and a predominantly stromal region (fibrous tissue, fat, lymphocytes) with minor cancerous infiltration (right corner, ROI2).Consistent with our observations in primary HER2-positive breast tumors (Fig. 1H-J), these results indicate that lymphocyte-infiltrated regions within lung metastases may serve as preferential sites for the co-localization of these two subpopulations.

To assess the spatial proximity between cell phenotypes, we utilized the "From-with" analysis from the phenoptrReports package. This metric was used to quantify the number of $CD8A^+ABCA12^+$ T cells located within a defined radius of $PROM1^+SLC27A4^+$ tumor cells. The results revealed that the count of $CD8A^+ABCA12^+$ cells near $PROM1^+SLC27A4^+$ cells was significantly higher in ROI1 and ROI2 compared to other regions (**Fig. 7D-E**). This finding confirms the distinct regional enrichment of these two subpopulations, particularly within the lung bronchus and lymphocyte-infiltrated zones. To further quantify their spatial association, we used the "Within mean" metric. This metric estimates the average number of $PROM1^+SLC27A4^+$ tumor cells surrounding each $CD8A^+ABCA12^+$ T cell within a defined radius. Results (**Fig. 7F-G**) suggested that the number of $PROM1^+SLC27A4^+$ cells surrounding $CD8A^+ABCA12^+$ cells was significantly higher in ROI2 and ROI3.

Within the breast cancer lymph node metastases, we delineated five key regions based on the co-distribution of $CD8A^+ABCA12^+$ and $PROM1^+SLC27A4^+$ cells and the strength of their spatial association (**Fig. 7H-I**). Analysis of the panoramic spatial distance heatmap (**Fig. 7J**) revealed that the two subpopulations were in closer proximity in the catheter and necrotic tissue (ROI1) and in the necrotic tissue (ROI2). Consistent with our findings in Fig. 1H-J, both subpopulations also localized within necrotic regions. Collectively, these results reinforce that these two subpopulations exhibit region-specific enrichment with marked differences in necrotic areas. Both "From with" (**Fig. 7K-L**) and "Within mean" (**Fig. 7M-N**) analyses confirmed that $PROM1^+SLC27A4^+$ and $CD8A^+ABCA12^+$ cells form intimate spatial associations, specifically in ROI1 (necrotic regions) and ROI4 (periductal stroma), suggesting that necrotic and periductal regions may represent spatial niches where these subpopulations preferentially accumulate in lymph node metastases.

The enrichment of these subpopulations in lymphocyte-infiltrated and necrotic areas suggests cancer cells may counter-attack T cells to induce immunosuppression, while necrotic zones could be a source of tumor recurrence. Furthermore, their presence in ductal structures of the lung bronchi and lymph nodes raises the possibility that ductal or peribronchial structures may represent permissive anatomical sites for niche establishment.

2.8 Spatial *in situ* analysis of breast tumor metastasis and chemoresistance linked to the exhaustion gradient of $CD8A^+ABCA12^+$ subpopulations

Beyond the metastatic events previously described, we shifted our investigation to an earlier time point: the formation of the intravascular tumor embolus niche during the initial stages of dissemination. In breast cancer patients, a histopathological manifestation associated with metastatic dissemination are typically characterized by the spread of cells from the primary tumor to lymph nodes, a process that forms distinct pathological clusters known as lymphovascular tumor emboli. Therefore, we investigated the enrichment of key subpopulations within these vascular tumor emboli to determine their potential role in the

initial stages of metastatic spread. Since chemotherapy-induced resistance often promotes the expansion of tumor-initiating cells, and our PROM1$^+$SLC27A4$^+$ subpopulation exhibits stemness characteristics (SFig. 1E-G), it was critical to assess their behavior in this context.

First, we focused on a cohort of breast cancer patients with lung metastasis, including those with or without chemotherapy, analyzing the distribution of the two subpopulations within the dense embolic niches of primary breast tumors and lymph nodes. Spatial neighbor analysis using Euclidean distance metrics showed that both CD8A$^+$ITGAE$^+$ and CD8A$^+$ABCA12$^+$, especially the latter, were localized in close proximity to PROM1$^+$SLC27A4$^+$ cells (**Fig. 8A-H**). Using the spatial coordinates from these emboli, we constructed local differentiation trajectories to quantify the spatiotemporal distance between putative state 0 (CD8A$^+$ITGAE$^+$) and state 1 (CD8A$^+$ABCA12$^+$) subclusters (**Fig. 8I-J, 8P-Q**). Differentiation trees were generated to visualize a clear transition from CD8A$^+$ITGAE$^+$ cells (teal regions) to CD8A$^+$ABCA12$^+$ cells (ginger regions) (**Fig. 8K, 8R**). We also identified transition genes, most notably *TIGIT*, defined by their monotonic expression shifts along the differentiation path (**Fig. 8L-O, 8S-V**).

Next, we performed 10X Xenium in situ analysis on lymphovascular tumor emboli from 21 paired primary tumor and lymph node samples of HER2-positive breast cancer patients. The cohort was structured to account for chemotherapy administration and subsequent lung metastasis occurrence. Our findings pinpointed chemotherapy and lung metastasis as two key factors driving the enrichment of both CD8A$^+$ABCA12$^+$ and CD8A$^+$ABCA12$^+$TIGIT$^+$ subpopulations. Chemotherapy significantly increased their abundance regardless of metastatic outcome (**SFig. 3A-B, E-F**). Concurrently, patients who developed lung metastasis consistently showed higher enrichment of these cells, both with (**SFig. 3D, H**) and without (**SFig. 3C, G**) chemotherapy.

Taken together, these findings suggest a dynamic process within the cancer emboli of early-stage metastatic breast cancer. Both CD8A$^+$ITGAE$^+$ and CD8A$^+$ABCA12$^+$ cells were found in close proximity to PROM1$^+$SLC27A4$^+$ cancer cells, especially the latter. The identification of *TIGIT* as a key transition gene in the state transition from CD8A$^+$ITGAE$^+$ to CD8A$^+$ABCA12$^+$ links this TRM-like cell evolution to an exhausted state. Therefore, the significant enrichment of these exhausted CD8A$^+$ABCA12$^+$TIGIT$^+$ cells in emboli from patients with lung metastasis or chemotherapy treatment strongly associates this exhausted T-cell state with metastatic progression and chemoresistance.

3. Discussion

The present study employed an integrated spatial multi-omics approach, combined with functional assays and clinical validation, to dissect the role of CD8$^+$ T cell subsets in supporting tumor-initiating cell (TIC) survival and progression in HER2-positive breast cancer. Our key findings are threefold: (1) We identified a previously uncharacterized exhausted CD8A$^+$ABCA12$^+$ T cell subset that is reprogrammed by PROM1$^+$SLC27A4$^+$ TICs to construct post-chemotherapy-enriched and metastatic progression-associated niches; (2) The EGF-EGFR-STAT5 signaling axis and fatty acid metabolic pathway (from ABCA12-mediated efflux, then SLC27A4-dependent uptake, to PDM formation, and MFN2/ATP upregulation) form the molecular basis of this TIC-CD8A$^+$ABCA12$^+$ crosstalk; (3) CD8A+ABCA12+ cells, whose transcriptional features are consistent with a putative

origin from TRM CD8A+ITGAE+ T cells, are enriched in high-grade/metastatic lesions (especially lymph node emboli) and post-chemotherapy samples, and correlate with poor prognosis. These results address critical gaps in our understanding of TME-TIC interactions and provide new insights into HER2-positive breast cancer progression. These are summarized in ink painting-style graphs (**SFig. 4**).

The metastatic cascade exerts rigorous selective constraints—including resistance to anoikis, evasion of immune surveillance, and escape from cellular dormancy—that selectively enrich for cells endowed with strong self-renewal activity and stress-tolerance programs, both of which are defining features of the TIC state. Accordingly, the prominent accumulation of PROM1$^+$SLC27A4$^+$ TICs in lymph node and lung metastases does not conflict with their classification as TICs; instead, it provides the enrichment of PROM1$^+$SLC27A4$^+$ TICs in lymph node and lung metastases is consistent with the possibility that this population contains metastasis-initiating-like cells. The designation "TIC" reflects their functional clonogenic potency in experimental assays, whereas our metastatic data illuminate their biological role in driving clinical disease progression. This dual functionality aligns with the well-established paradigm that metastasis is an inherently inefficient process that necessitates the re-establishment of tumor growth at distant organ sites—a capacity restricted to a minor subpopulation of cells possessing TIC-like properties.

Prior studies have established that TICs rely on "ecological niches" to evade therapy and metastasize, but these niches were primarily attributed to stromal cells (e.g., cancer-associated fibroblasts) or vascular components [6,7]. Our work extends this paradigm by demonstrating that exhausted CD8$^+$ T cells—traditionally viewed as passive bystanders of anti-tumor immunity—are active contributors to TIC niche formation. This aligns with emerging evidence that tumors "hijack" immune cells for progression [11], but advances it by identifying a subset-specific role: unlike general CD8$^+$ T cell exhaustion (marked by PD-1 alone [8]), CD8A$^+$ABCA12$^+$ cells uniquely combine immune hypofunction (TIGIT upregulation) with metabolic support (ABCA12-mediated fatty acid efflux) for TICs.

The limited efficacy of PD-1 blockade in HER2-positive breast cancer is likely multifactorial, including tumor mutational burden, immunosuppressive stromal composition, and T cell intrinsic factors [11]. Our data raise the additional possibility that the metabolic support provided by CD8A$^+$ABCA12$^+$ cells to PROM1$^+$SLC27A4$^+$ TICs may represent a previously unrecognized resistance mechanism that is not addressed by PD-1 blockade alone. Our identification of the EGF-EGFR-STAT5 axis as a regulator of CD8A$^+$ABCA12$^+$ cell function also fills a knowledge gap. While EGF-EGFR signaling is well-documented in TIC self-renewal [23], its role in TIC-immune cell crosstalk remains understudied. We show that TIC-secreted EGF not only activates STAT5 in CD8A$^+$ABCA12$^+$ cells but also may contribute to concurrent upregulation of TIGIT (immune exhaustion) and ABCA12 (metabolic support)—a "one-signal, two-effect" mechanism that efficiently reprograms CD8$^+$ T cells toward a niche-supporting phenotype. This is particularly notable given that STAT5 is often associated with T cell activation [24]; our data reveal a context-dependent role for STAT5 in promoting T cell exhaustion, highlighting the TME's ability to rewire canonical signaling pathways.

The metabolic crosstalk we uncovered—CD8A$^+$ABCA12$^+$ cells promote ABCA12-dependent lignoceric acid release that are taken up by TICs to form PDM—adds a new

layer to TIC niche biology. PDMs are specialized mitochondrial structures that enhance lipid oxidation and ATP production under nutrient stress [25], and our finding that TICs exploit $CD8A^+ABCA12^+$ cells to acquire fatty acids for PDM formation explains their enhanced bioenergetic programs associated with drug tolerance and metastatic potential. This aligns with reports that TICs rely on exogenous nutrients to sustain their high energy demands [26] but identifies $CD8^+$ T cells as an unexpected metabolic "donor"—a departure from the traditional view that immune cells compete with cancer cells for nutrients [27].

From a clinical perspective, our findings provide three actionable insights. First, the enrichment of $CD8A^+ABCA12^+$ cells in high-grade HER2-positive lesions, lymph node/lung metastatic foci, and post-chemotherapy samples identifies this subset as a potential prognostic biomarker. Unlike existing markers (e.g., PD-L1 [28]), $CD8A^+ABCA12^+$ cells directly reflect the functional state of the TIC niche, making them a more specific indicator of treatment response and metastasis risk. For example, patients with high $CD8A^+ABCA12^+$ infiltration post-chemotherapy may benefit from adjuvant therapies targeting this subset, while those with low infiltration may have better outcomes with standard anti-HER2 regimens. Second, our mechanistic data suggest previously uncharacterized potential therapeutic vulnerability for overcoming resistance. Targeting the EGF-EGFR-STAT5 axis (e.g., EGFR inhibitors like gefitinib [29] or STAT5 inhibitors [30]) could block $CD8A^+ABCA12^+$ cell reprogramming, while inhibiting ABCA12 (e.g., small-molecule efflux inhibitors [31]) or SLC27A4 (e.g., anti-SLC27A4 antibodies [32]) would disrupt fatty acid transfer to TICs. Importantly, these strategies could be combined with immune checkpoint blockade (ICB): by reversing $CD8A^+ABCA12^+$ exhaustion (via TIGIT inhibition [33]) and blocking metabolic support, dual targeting may restore anti-tumor immunity while depriving TICs of their niche. This is particularly relevant for HER2-positive breast cancer, where ICB monotherapy has shown modest efficacy [34]. Third, the putative differentiation trajectory of $CD8A^+ABCA12^+$ cells from TRM $CD8A^+ITGAE^+$ cells suggest a preventive opportunity. TRMs are long-lived cells that populate tissues and mediate local immunity [35]; our data imply that chronic tumor inflammation (driving immune scarring [2]) converts protective TRMs into niche-supporting $CD8A^+ABCA12^+$ cells. Intervening early to preserve TRM function—e.g., targeting inflammatory mediators that trigger this state transition—could prevent niche formation before TICs establish resistance.

In addition to its prognostic and therapeutic implications, our spatial analysis may also provide a pathological perspective for interpreting tumor necrosis. Necrotic regions are clinically important in breast cancer evaluation, but their assessment can be influenced by sampling variation, tissue preservation, and interobserver differences, particularly when necrosis is focal, intraductal, or spatially heterogeneous. In our multiplex immunofluorescence analysis, regions with a dense exhaustion gradient between $CD8A^+ABCA12^+TIGIT^-$ and $CD8A^+ABCA12^+TIGIT^+$ cells were frequently observed in necrotic areas, especially intraductal and intraluminal necrosis. This finding suggests that necrosis may not merely represent passive tissue destruction but may also reflect a local immunometabolic state characterized by progressive T cell exhaustion and TIC-supportive niche remodeling. Therefore, integrating spatial immune-exhaustion patterns with conventional histopathological assessment may provide additional information for defining necrotic regions, evaluating tumor aggressiveness, and predicting disease progression.

Future studies with larger pathological cohorts are needed to determine whether exhaustion-gradient mapping can improve the reproducibility and clinical utility of necrosis assessment.

Recent failures of TIGIT-targeted therapies indicate that TIGIT expression alone may be insufficient for patient selection. Our data suggest that TIGIT should be interpreted within a subset-specific and metabolic context, particularly in $CD8A^{+}ABCA12^{+}$ cells coupled to $PROM1^{+}SLC27A4^{+}$ TICs. This may help explain why non-selective TIGIT blockade has limited efficacy and suggests that TIGIT inhibition may require combination with strategies disrupting EGFR-STAT5 signaling or lipid-transfer pathways.

Despite these strengths, our study has several limitations. A question raised by our findings is whether the $PROM1^{+}SLC27A4^{+}/CD8A^{+}ABCA12^{+}$ crosstalk is truly specific to HER2-positive breast cancer or instead represents a broader tumor ecological program. Although the present study was designed and validated in HER2-positive clinical samples and models, our current data do not support a definitive claim of absolute subtype exclusivity. Given that both EGF-EGFR signaling and fatty acid metabolic reprogramming are recurrent features across multiple malignancies, similar TIC-immune interactions may also occur in other breast cancer subtypes, including TNBC or Luminal disease. However, several features may make this axis particularly prominent in HER2-positive tumors: the strong dependency on growth factor signaling networks, the high degree of therapy-driven selective pressure, and the marked metabolic plasticity associated with HER2-driven tumor-initiating cells. We therefore interpret this mechanism as currently best supported in HER2-positive breast cancer, while acknowledging that future cross-subtype studies integrating spatial transcriptomics, single-cell profiling, and functional validation will be required to determine whether this crosstalk is HER2-restricted, HER2-enriched, or a more general feature of aggressive breast cancer.

In summary, our study identifies $CD8A^{+}ABCA12^{+}$ cells as a critical mediator of TIC niche formation in HER2-positive breast cancer, uncovering a previously uncharacterized "immune hijacking" mechanism that combines signaling reprogramming and metabolic crosstalk. These findings not only advance our understanding of TME-TIC interactions but also provide a rationale for targeting the $CD8A^{+}ABCA12^{+}$ subset to improve precision therapy for HER2-positive breast cancer—addressing the long-standing clinical challenge of drug resistance and metastasis.

4. Declarations

Ethics approval and consent to participate

Human research was approved by Medical Ethics Committee of Shanghai General Hospital (No.:2021SQ203). All patients provided written informed consent.

Consent for publication

Not applicable

Availability of data and materials

Processed sequencing data were deposited in National Genomics Data Center (accession:

OMIX006245). The datasets used and/or analysed during the current study are available from the corresponding author on reasonable request.

Competing interests

The authors declare that they have no competing interests.

Funding

This study was supported by grants from National Natural Science Foundation of China, No. 81601985, No. 82173171, No. 82372904, Scientific research project of Shanghai Municipal Health Commission(20214Y0094), Scientific research project of Weifang Municipal Health Commission (WFWSJK-2025-132). All the funding bodies are used for the design of the study and collection, analysis and interpretation of data and in writing the manuscript

Authors' contributions

Sample arrangement, transportation and personnel coordination: Zhang YX., Fu XN., Hong L. Single-nucleus analysis: Yin HJ. Spatial transcriptome analysis: Yin HJ., Liu HY., Fu XN. Spatial metabolomics analysis: Yin HJ., Fu XN. Spatial protein analysis: Yin HJ., Fu XN., Zhang ZK., Yang XF. Clinical pathology slide preparation, analysis and statistics: Yin HJ., Zhang YX., Hong L, Li YT., Dong XT. Molecular mechanism experiments: Yin HJ., Wang W. Animal experiments: Yin HJ., Lv YC., Li W., Liang WH. Fluorescence-based experiments: Yin HJ., Jin W., Gao TL. Electron microscopy sample preparation and analysis: Yin HJ., Sun Y., Han GY., Li Z. Original design and drawing of article figures: Yin HJ., Wang W. Original ideas for articles: Yin HJ. Writing and advanced polishing: Yin HJ., Zheng DW, Wang W.Allocation of funds and human resources: Yin HJ.

Acknowledgments

We thank ZEISS Microscopy Customer Center (Shanghai) for their assistance with our Volume EM experiments using the Crossbeam 550 system.

Methods and Material

1. Sample Utilization and Experimental Design

All patients provided written informed consent. Samples were allocated as follows: 1) Single-Nucleus RNA Sequencing: Nuclei from fresh tissues of 20 HER2-positive breast cancer patients for sequencing. 2) Spatial Transcriptomics and Metabolomics: Concurrent analyses on fresh tissues of 6 patients. 3) Spatial Proteomics and Regional Characterization: Tissues from 12 patients with preserved pathology for relevant analyses. 4) Spatial *In Situ* Analysis: 21 pairs of samples (primary tumor foci and lymph node metastatic tumor embolus niches) from patients. 5) Experimental Validation and Mechanistic Studies: Tissues from 12 patients (excluding damaged samples unsuitable for experiments).

2. Single-nuclear transcriptome sequencing and quality control

Single-nuclear transcriptome sequencing

Nuclei were resuspended in PBS with 1% BSA, viability assessed via trypan blue staining, adjusted to 1000-1200/μl, and cDNA libraries amplified using 10XGenomics Chromium Next GEM Single Cell 3' Reagent Kits v3.1. Libraries were constructed with Chromium™ Single Cell 3' Library Construction Kit and sequenced on Illumina Nova 6000 (PE150 mode).

Sequencing data quality control and gene quantification

Library construction, sequencing, and data analysis were performed by OE Biotech Co., Ltd. Raw fastq data were quality-checked using Cell Ranger[16] (integrating STAR), aligned to GRCh38 reference genome (link: https://cf.10xgenomics.com/supp/cell-exp/refdata-gex-GRCh38-2020-A.tar.gz).

Gene quantitative quality control and data preprocessing

Seurat [17] 4.0.0 was used for further quality control: high-quality cells were filtered by nGene > 200, nUMI > 1000, log10GenesPerUMI > 0.7, mitochondrial UMI proportion < 5%, and red blood cell gene proportion < 5%. Doublet Finder [18] was used for doublet removal.

3. Single-nuclear transcriptome sequencing and advanced bioinformatics analysis

Dimensionality reduction and clustering analysis

Highly variable genes (HVGs) were screened via Seurat's Find Variable Genes. Principal component analysis (PCA) was performed on HVG expression profiles, with batch effects removed using mutual nearest neighbors (MNN). SNN clustering was visualized by UMAP.

Marker gene identification

Marker genes for each cell cluster were identified using Seurat's Find All Markers and visualized via Violin Plot and Feature Plot.

Differential genes and enrichment analysis

Differential genes were screened by Seurat's Find Markers ($p < 0.05$, fold change > 1.5) and subjected to GO/KEGG enrichment analysis via hypergeometric distribution test.

Pseudo time analysis

Monocle2[19] v2.9.0 was used for cell differentiation trajectory inference: Seurat objects converted to Cell Data Set, ordering genes filtered (qval < 0.01), dimensionality reduction

clustering performed, and trajectory inferred via order Cells.

Cell Phone DB cell communication analysis

Cell Phone DB [20] v3.0 identified ligand-receptor pairs. Genes expressed in ≥10% of cells in a cell type were analyzed; cell type markers were permuted 1000 times to generate null distributions and calculate p-values. Finally, the R packages Igraph and Circlize were used for network visualization.

GSVA enrichment analysis

KEGG background gene sets were obtained via GSEA Base v1.44.0. GSVA v1.30.0 scored pathway activity, and LIMMA v3.38.3 analyzed pathway activity differences between groups.

4. Spatial transcriptomics

stSME Standardization and Clustering

stSME in stLearn [24] integrated gene expression, tissue morphology, and spatial location. Stained images were segmented, ResNet50 extracted 2084-dimensional features (PCA to 50 PCs). Morphological distances were calculated via cosine distance; gene expression was normalized by SME. Global clustering (gene expression-based) and local density clustering (spatial information-based) were performed.

Pseudo-Spatial-Temporal Analysis (PST)

The Pseudo-Spatial-Temporal (PST) analysis detects biological processes inferable from transcriptional state gradients across tissues [25-27]. It reconstructs evolutionary trajectories based on cellular spatial environment and transcriptomic profiles within tissues. Post-SMEclust analysis, PST identifies both local tissue-level (relationships between subgroups of individual cell subpopulations) and global-level (relationships between subpopulations) connections. The algorithm overview is as follows: (1) Trajectory Analysis: stLearn first applies PAGA trajectory analysis to SME-normalized gene expression data across the entire tissue to reveal intra-subpopulation connections. (2) Diffusion Pseudo Time (DPT) Calculation: The robust DPT method, adopting a random walk-like approach to measure cell-to-cell transitions, is then used to compute pseudo time values; users can define root nodes for directional trajectories based on the target biological process. (3) Pseudo-Spatial Distance Calculation: Finally, the algorithm integrates gene expression values and physical distances to calculate the pseudo-space-time distance (PSTD), constructs a directed graph, and optimizes it via the directed minimum spanning tree algorithm to identify the shortest rooted tree and connecting branches.

5. Spatial metabolomics

Chemicals, Reagents, and Instruments

MS-grade acetonitrile (Thermo Fisher), purified water (Watsons), formic acid (Merck), tissue freezing medium (Leica), Eosin Y-solution, Hematoxylin (Sigma-Aldrich); Leica CM 1950 Cryostat Microtome, Optical Microscope (Phoenix), Superfrost Plus Slides (Thermo Fisher), DESI XS Imaging Platform, Synapt XS Mass Spectrometer (Waters), Freeze Dryer.

Sample preparation

-80 °C stored embedded samples were cut into 10 μm sagittal slices (10 slices) via cryostat microtome, mounted on positive charge desorption plates, and stored at -80 °C. Slices were desiccated at -20 °C for 1 h and room temperature for 2 h before MSI; adjacent

slices were used for H&E staining.

Data acquisition and MSI analysis

The analyses were performed as previously reported [28]. In brief, AFADESI-MSI platform coupled with Q-Orbitrap mass spectrometer was used. Spray solvent: ACN/H2O (8:2) (positive/negative ion mode), flow rate 5 μL/min, transporting gas 45 L/min, spray voltage 7 kV, distances 3 mm. MS parameters: resolution 70,000, mass range 70-1000 Da, AGC target 2E6, max injection time 200 ms, S-lens voltage 55 V, capillary temperature 350 °C. Scanning rate 0.2 mm/s (x-direction), step 100 μm (y-direction).

Data Processing

Collected ". raw" files were converted to ".imzML" format via imzML Converter [29], then imported into MSiReader (a Matlab-based open-source interface for high-resolution MS imaging file analysis) for ion image reconstruction following background subtraction with Cardinal [30]. All MS images were normalized by pixel-wise total ion count (TIC) [31]. Region-specific MS profiles were accurately extracted by matching high-spatial-resolution H&E images. Orthogonal partial least squares discrimination analysis (OPLS-DA), a supervised statistical method, was used to screen discriminative endogenous molecules across different tissue microregions. Variable Importance of Projection (VIP) values from the OPLS-DA model ranked the contribution of each variable/metabolite to group discrimination, with VIP > 1 indicating potential differential metabolites. Subsequent two-tailed Student's T-test verified statistical significance, and differential metabolites were finalized with VIP > 1.0 and $p < 0.05$.

Additionally, for the specific MSI data structure, T-distributed stochastic neighbor embedding (t-SNE) and uniform manifold approximation and projection (UMAP) were performed for pixel-wise MS data dimensionality reduction. Spatial shrunken centroids clustering (SSCC) was applied to cluster MSI data based on inter-pixel ion abundance differences for sample separation.

Analyte Identification

The ions detected by AFADESI were annotated by the pySM [32] pipeline and an in-house SmetDB database (Lumingbio, Shanghai, China).

6. Integrated analysis of spatial metabolomics and spatial transcriptomics

The barcode spatial information of spatial transcriptomics and pixel data of spatial metabolomics were converted into unified spatial identifiers. Metabolomic pixel points were linked to transcriptomic spots by summing the ion data of corresponding pixels per spot, yielding metabolomic data matching each transcriptomic spot via this integration.

The specific process is as follows: 1) Prerequisite: Samples for both analyses are from adjacent tissue sections with consistent microstructural contours. 2) Match sample microstructural contours. 3) Select 6 anchor points to establish a new coordinate system. 4) Calculate metabolomic pixel coordinates. 5) Convert metabolomic data into the format of spatial transcriptomics. 6) Confirm cell type spot information (including microregion data and gene-positive/negative area verification). 7)-1. Screen marker metabolites in the target region. 7)-2. Analyze differential metabolites in the target region. 8) Conduct joint pathway analysis.

7. Spatial proteomics

ROI segmentation, image unmixing, and panoramic stitching

Phenochart was used to define whole-slide ROIs. inForm was used for spectral unmixing and data export. QuPath-Merge files were stitched using the pyramid.groovy script.

Spatial Biology Analysis Workflow with inForm and PhenoptrReports

Multispectral images were unmixed and segmented in inForm to obtain cell objects for phenotypic analysis. Data tables and images were exported. phenoptrReports was used to merge data, generate consolidated tables, and visualize spatial relationships via Spatial Map Viewer.

To quantify cell-to-cell spatial proximity, the "From-with" and "Within mean" metrics in phenoptrReports were used. The "From-with" analysis quantifies the number of "From" cells that have at least one "To" cell within a defined radius, thereby evaluating spatial adjacency between two phenotypes. In this study, $CD8A^{+}ABCA12^{+}$ T cells were defined as the "From" cells and $PROM1^{+}SMAD5^{+}$ tumor cells as the "To" cells. A higher "From-with" count indicated stronger spatial proximity between the two populations.

The "Within mean" metric was used as a complementary measurement to calculate the average number of "To" cells surrounding each "From" cell within a defined radius. Specifically, this metric quantified the average number of $PROM1^{+}SMAD5^{+}$ tumor cells located around each $CD8A^{+}ABCA12^{+}$ T cell, reflecting the local clustering intensity between the two cell populations.

QuPath Segmentation, and Phenotype Analysis

Stitched images were imported into QuPath; ROIs defined, StarDist script for cell segmentation. Training images were created, classifiers trained, and applied to original images. Spatial distances to specific phenotypes were calculated and visualized..

CytoMAP Cell Neighborhood Analysis

QuPath cell data were exported as .csv. CytoMAP loaded data, defined cell phenotypes via ch_Class annotation. 50 μm raster-scanned neighborhoods were set to count cell types; neighborhoods were clustered, and interactions analyzed with heatmaps and networks.

Cell Neighborhood Interactions

To analyze cell neighborhood interactions, select the neighborhood clustering model via "Region Interactions" and generate composition heatmaps and interaction networks for multi-dimensional characterization. The heatmap shows specific proportional values; in the network, circle size denotes neighborhood cell count, while straight line thickness indicates the proportion of shared boundaries between neighborhoods (thicker lines mean higher proportions).

8. Experimental Procedures

Ultra-multiplexed immunohistochemistry experiment

Primary antibody specificity was validated via IHC (SABC, DAB). Opal 6-Plex Manual Detection Kit stained paraffin tissue microarrays (dewaxing, hydration, 10% neutral formalin fixation, microwave antigen retrieval, blocking, primary antibody incubation, Opal HRP/working solution treatment). Cycles depended on antibody quantity. Mounting with ProLong Diamond antifade mountant and coverslips; panoramic scanning via Vectra

Polaris, images analyzed with Phenochart 1.1.0.

Single cell collection for human samples

Surgical samples were placed in protection solution (Miltenyi Biotec), cut into 1 mm^3 pieces, transferred to gentleMACS C Tubes (Miltenyi Biotec) with diluted digestion enzyme (Human Tumor Dissociation Kit, Miltenyi Biotec), and processed via gentleMACS program h_tumor_01 (37 °C water bath, 30 min, repeated twice). Cell suspension was filtered (70 μm strainer), centrifuged (300 g, 7 min), and processed for red blood cell lysis if needed.

Flow cytometry analysis

Miltenyi Biotec's Dead Cell Removal Kit pre-filtered dead cells to avoid multicolor FCM staining interference. For intracellular cytokine detection (article figure), cells were stimulated 2 h at 37℃ in 10% heat-inactivated FBS-supplemented 1640 medium (plus stimulation cocktail and protein transport inhibitors), then fixed, permeabilized, washed, and stained. Nuclear indicators (article figure) used Thermo Fisher's Transcription Factor Staining Buffer Set per protocol; surface-cytoplasm-nucleus staining order was followed for multi-location marker panels.

Pre-run, BD Fortessa was calibrated with BD's CS&T beads (Diva7.0) for QC. Fluorescence compensation for mouse/human panels was adjusted via Thermo Fisher's UltraComp eBeads and BD's Anti Ms Ig CompBead Plus Set. Labeled cells were resuspended in 400 μl staining buffer and transferred to BD FACS tubes (352054). Low-cell human tissue samples used Corning 1.2ml tubes (4401) for density maintenance; viscous post-dissociation samples (unimproved by DNase) were filtered with BD FACS tubes (352235) for immediate analysis.

Electron Microscopy (EM)

Sample preparation for EM: Samples were immediately fixed in 2.5% glutaraldehyde, 1% formaldehyde, and 0.1 M phosphate buffer (pH 7.4) overnight, then sliced into two parts for LM and EM (orientation recorded). EM samples were washed with 0.1 M phosphate buffer, incubated in 1.5% K3[Fe(CN)6] with 2% OsO4 on ice for 1 h, followed by TCH solution (20 min, room temperature) and 2% OsO4 (30 min, ice) with washing steps. Samples were stained with 1% uranyl acetate (4 °C, overnight) and Walton's lead aspartate (60 °C, 30 min), washed, dehydrated (graded alcohol, acetone), infiltrated with epoxy resin (50%, 75%, 100%), and embedded at 60 °C for 48 h. Polymerized blocks were trimmed and glued to stubs for FIB-SEM.

FIB-SEM imaging: ZEISS Crossbeam 550 with Atlas 5 software was used (1.5 keV, 1 nA, working distance 5.0 mm, pixel size 10×10 nm). FIB milling (30 keV, 700 pA, 10 nm thickness). Image stacks were aligned via Atlas 5 and exported as TIFF.

Image analysis: Representative images were uploaded to ZEISS arivis Cloud to train AI models (nuclei, mitochondria, lipid droplets). Image stacks were segmented in arivis Pro (manual corrections if needed) for 3D reconstruction and quantitative analysis [36].

9. Pathology methods, clinical specimens and statistical analysis

Pathology methods

Tumor histological grade was classified via Elston and Ellis scoring system. IHC (Ventana BenchMark XT) stained ER, PR, HER2, Ki-67 on 4-μm FFPE slices. HER2 IHC scoring: 0, 1^+, 2^+, 3^+; FISH was performed for IHC 2^+. Two pathologists evaluated slides.

ER/PR positivity: ≥1% nuclear staining; HER2 positivity: IHC 3^+ or FISH amplified; Ki-67 index: percentage of positive nuclei (≥1000 invasive cells). All histologic and IHC tumor slides were evaluated by two pathologists. Histological grades and all biological features were evaluated based on the invasive components.

Clinical specimens

The baseline data including age and tumor characteristics (tumor size, lymph node metastasis, tumor grade, pathological stage, ER/PR/HER2 expression) were collected. All patients provided written consent. Studies were approved by the the Committees for Ethical Review of Research involving Human Subjects of our institute.

Statistical analysis

Categorized variables: Chi-Square test. Survival analysis: Log-rank test and Cox regression. Between two groups: Student's t-test; multiple groups: one-way ANOVA. Non-normal/distributed heterogeneous data: Mann-Whitney U test/Rank test. Fisher's exact test was used if necessary. $p < 0.05$ was significant. Analyses were performed in SPSS 17.0 and Graphpad Prism 8. Data are presented as mean ± SEM.

Reference

[1] Gerstung M, Jolly C, Leshchiner I, et al. The evolutionary history of 2,658 cancers. Nature, 2020; 578: 122-128.

[2] Azizi E, Carr AJ, Plitas G, et al. Single-cell map of diverse immune phenotypes in the breast tumor microenvironment. Cell, 2018; 174(5): 1293-1308.

[3] Slamon DJ, Leyland-Jones B, Shak S, et al. Use of chemotherapy plus a monoclonal antibody against HER2 for metastatic breast cancer that overexpresses HER2. N Engl J Med, 2001; 344: 783-792.

[4] Di Leo A, Isola J, Pietras K, et al. HER2-positive breast cancer: an evolving landscape of care. Nat Rev Clin Oncol, 2017; 14: 633-649.

[5] Guarneri V, Curigliano G. Metastatic HER2-positive breast cancer: current and future treatment strategies. Ther Adv Med Oncol, 2019; 11: 1758835919862768.

[6] Pece S, Tosoni D, Confalonieri S, et al. Biological and clinical implications of cancer stem cells. Nat Rev Clin Oncol, 2010; 7: 314-325.

[7] Batlle E, Clevers H. Cancer stem cells revisited. Nat Med, 2017; 23: 1124-1134.

[8] Li C, Liu SW, Yan RP, et al. CD54-NOTCH1 axis controls tumor initiation and cancer stem cell functions in human prostate cancer. Theranostics, 2017; 7(1): 67-80.

[9] Fang C, Fan CW, Wang C, et al. Prognostic value of $CD133^{+}CD54^{+}CD44^{+}$ circulating tumor cells in colorectal cancer with liver metastasis. Cancer Med, 2017; 6(12): 2850-2857.

[10] Li H, Anne ML, Ido Y, et al. Dysfunctional CD8 T cells form a proliferative, dynamically regulated compartment within human melanoma. Cell, 2019; 176: 775-789.

[11] Patten DK, Corleone G, Győrffy B, et al. Enhancer mapping uncovers phenotypic heterogeneity and evolution in patients with luminal breast cancer. Nat Med, 2018; 24(9): 1469-1480.

[12] Maynard A, McCoach CE, Rotow JK, et al. Therapy-induced evolution of human lung cancer revealed by single-cell RNA sequencing. Cell, 2020; 182: 1232-1251.

[13] Pham DT, Tan X, Xu J, et al. stLearn: Integrating spatial location, tissue morphology, and gene expression to find cell types, cell-cell interactions, and spatial trajectories within undissociated tissues. bioRxiv, 2020.

[14] Beltra JC, Manne S, Abdel-Hakeem MS, et al. Developmental relationships of four exhausted $CD8^{+}$ T cell subsets reveals underlying transcriptional and epigenetic landscape control mechanisms. Immunity, 2020; 52(5): 825-841.e8.

[15] Chu X, Tian W, Wang Z, et al. Co-inhibition of TIGIT and PD-1/PD-L1 in cancer immunotherapy: mechanisms and clinical trials. Mol Cancer, 2023; 22(1): 93.

[16] Banta KL, Xu X, Chitre AS, et al. Mechanistic convergence of the TIGIT and PD-1 inhibitory pathways necessitates co-blockade to optimize anti-tumor $CD8^{+}$ T cell responses. Immunity, 2022; 55(3): 512-526.e9.

[17] Freed-Pastor WA, Lambert LJ, Ely ZA, et al. The CD155/TIGIT axis promotes and maintains immune evasion in neoantigen-expressing pancreatic cancer. Cancer Cell, 2021; 39(10): 1342-1360.e14.

[18] Cui J, Christin JR, Reisz JA, et al. Targeting ABCA12-controlled ceramide homeostasis inhibits breast cancer stem cell function and chemoresistance. Sci Adv, 2023; 9(48): eadh1891.

[19] Terrinoni A, Sala G, Bruno E, et al. Partial loss of function ABCA12 mutations generate reduced deposition of glucosyl-ceramide, leading to patchy ichthyosis and erythrodermia resembling erythrokeratodermia variabilis et progressiva (EKVP). Int J Mol Sci, 2023; 24(18): 13962.

[20] Gao S, Hu J. Mitochondrial fusion: the machineries in and out. Trends Cell Biol, 2021; 31(1): 62-74.

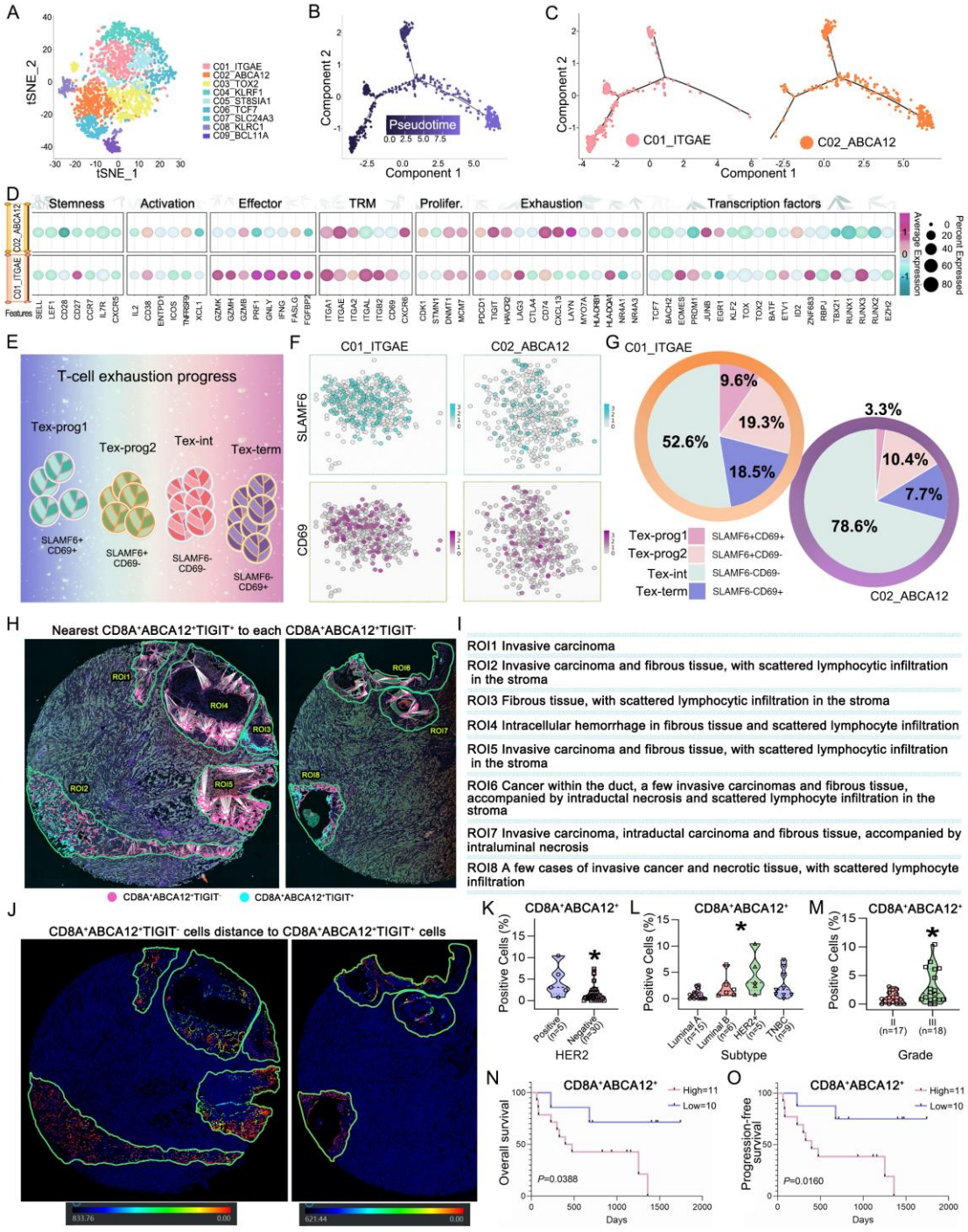
[21] Tábara LC, Burr SP, Frison M, et al. MTFP1 controls mitochondrial fusion to regulate inner membrane

quality control and maintain mtDNA levels. Cell, 2024; 187(14): 3619-3637.e27.
[22] Jiang Y, Krantz S, Qin X, et al. Caveolin-1 controls mitochondrial damage and ROS production by regulating fission-fusion dynamics and mitophagy. Redox Biol, 2022; 52: 102304.
[23] Yoo Y, Bae JS, Kim HJ, et al. EGF/EGFR signaling regulates cancer stem cell properties in triple-negative breast cancer. Exp Mol Med, 2020; 52(6): 967-978.
[24] Burchill MA, Lucas M, Joshi A, et al. STAT5 is a critical regulator of T cell function in health and disease. Front Immunol, 2020; 11: 583427.
[25] Rambold AS, Prats C, Haag M, et al. Perilipin 5 controls lipid droplet turnover and mitochondrial function in brown adipocytes and myocytes. J Cell Biol, 2015; 210(4): 603-618.
[26] Vietri M, Vacca A, Corazzari M, et al. Metabolic reprogramming of cancer stem cells: a therapeutic target. J Exp Clin Cancer Res, 2020; 39(1): 169.
[27] Chang CJ, Qiu J, O'Sullivan D, et al. Metabolic competition in the tumor microenvironment is a driver of cancer progression. Cell, 2015; 162(6): 1229-1241.
[28] Cortazar P, Park YH, de Azambuja E, et al. PD-L1 expression as a predictive biomarker in breast cancer. Nat Rev Clin Oncol, 2021; 18(10): 631-648.
[29] Ciardiello F, Tortora G. EGFR antagonists in cancer treatment. N Engl J Med, 2008; 358(11): 1160-1174.
[30] Hong JY, Lee HJ, Kim HS, et al. Targeting STAT5 in cancer: molecular mechanisms and clinical applications. Exp Mol Med, 2021; 53(10): 1599-1612.
[31] Sarkadi B, Ozvegy-Laczka C, Gottesman MM. ABC multidrug transporters: structure, function and role in chemoresistance. Biochim Biophys Acta, 2006; 1758(11): 1785-1803.
[32] Febbraio M, Silverstein RL. CD36: a class B scavenger receptor involved in angiogenesis, atherosclerosis, inflammation, and lipid metabolism. J Clin Invest, 2007; 117(11): 3055-3062.
[33] Johnston RJ, Comps-Agrar L, Kleinpeter S, et al. TIGIT and PD-1 dual blockade expands responsive populations of tumor-infiltrating T cells. Cancer Cell, 2018; 33(1): 146-159.e144.
[34] Schmid P, Adams S, Rugo HS, et al. Atezolizumab and nab-paclitaxel in advanced triple-negative breast cancer. N Engl J Med, 2018; 379(22): 2108-2119.
[35] Masopust D, Soerens AG. Tissue-resident memory T cells and fixed immune surveillance in nonlymphoid tissues. Immunity, 2019; 50(4): 886-900.
[36] Ajayi PT, Katti P, Zhang Y, et al. Regulation of the evolutionarily conserved muscle myofibrillar matrix by cell type dependent and independent mechanisms. Nat Commun, 2022; 13(1): 2661.

Figure Legend

Figure 1 Single-nucleus RNA sequencing (snRNA-seq) identified previously underappreciated exhausted T cell subpopulations in HER2-positive breast cancer

(A) tSNE visualization of nine T/NK cell subpopulations. (B) Pseudotime trajectories of C01_ITGAE and C02_ABCA12 subpopulations. (C) Alignment of all cell subpopulations onto pseudotime trajectories. (D) Dot plot emphasizes the marker gene expression patterns specific to the C01_ITGAE and C02_ABCA12 subpopulations. (E) Schematic of the SLAMF6/CD69-based exhaustion staging model. (F) Feature plots showing SLAMF6 and CD69 expression in C01_ITGAE and C02_ABCA12 subpopulations. (G) Quantification of SLAMF6 and CD69 expression and relative proportions of four exhaustion stages—Tex-prog1 ($SLAMF6^{+}CD69^{+}$), Tex-prog2 ($SLAMF6^{+}CD69^{-}$), Tex-int ($SLAMF6^{-}CD69^{-}$), and Tex-term ($SLAMF6^{-}CD69^{+}$)—in each subpopulation. (H) Spatial localization of $CD8A^{+}ABCA12^{+}TIGIT^{+}$ and $CD8A^{+}ABCA12^{+}TIGIT^{-}$ cells in the invasive carcinoma region of HER2-positive breast cancer, reconstructed from multiple regions of interest (ROIs) analyzed using phenoptrReports software. (I) Summary of the pathological features across eight major tissue regions. (J) TIGIT-based spatial stratification of $CD8A^{+}ABCA12^{+}$ T cells. Nearest-neighbor distances from $CD8A^{+}ABCA12^{+}TIGIT^{-}$ cells to $CD8A^{+}ABCA12^{+}TIGIT^{+}$ cells were assessed by cell segmentation and distance-based spatial heatmap analysis across multiple panoramic ROIs using QuPath. Heatmap scale ranges: 0-833.76 μm (left panel) and 0-621.44 μm (right panel); higher values indicate greater intercellular distances. (K-M) Correlation of $CD8A^{+}ABCA12^{+}$ cell proportion with clinicopathological characteristics, including HER2 status (K), molecular subtypes (L), and histological grade (M) (*$P < 0.05$). (N-O) Kaplan-Meier analysis of overall survival (N) and progression-free survival (O) stratified by $CD8A^{+}ABCA12^{+}$ cell proportion (median cutoff) in breast cancer patients.


A
tSNE_2
tSNE_1
C01_ITGAE
C02_ABCA12
C03_TOX2
C04_KLRF1
C05_ST8SIA1
C06_TCF7
C07_SLC24A3
C08_KLRC1
C09_BCL11A
B
Component 2
Component 1
Pseudotime
C
C01_ITGAE
C02_ABCA12
D
Stemness
Activation
Effector
TRM
Prolifer.
Exhaustion
Transcription factors
Average expression
Percent Expressed
Features
E
T-cell exhaustion progress
Tex-prog1
Tex-prog2
Tex-int
Tex-term
SLAMF6+ CD69+
SLAMF6+ CD69-
SLAMF6- CD69-
SLAMF6- CD69+
F
C01_ITGAE
C02_ABCA12
SLAMF6
CD69
G
C01_ITGAE
9.6%
19.3%
52.6%
18.5%
3.3%
10.4%
7.7%
78.6%
C02_ABCA12
Tex-prog1 SLAMF6+CD69+
Tex-prog2 SLAMF6+CD69-
Tex-int SLAMF6-CD69-
Tex-term SLAMF6-CD69+
H
Nearest CD8A+ABCA12+TIGIT+ to each CD8A+ABCA12+TIGIT-
ROI1
ROI2
ROI3
ROI4
ROI5
ROI6
ROI7
ROI8
CD8A+ABCA12+TIGIT-
CD8A+ABCA12+TIGIT+
I
ROI1 Invasive carcinoma
ROI2 Invasive carcinoma and fibrous tissue, with scattered lymphocytic infiltration in the stroma
ROI3 Fibrous tissue, with scattered lymphocytic infiltration in the stroma
ROI4 Intracellular hemorrhage in fibrous tissue and scattered lymphocyte infiltration
ROI5 Invasive carcinoma and fibrous tissue, with scattered lymphocytic infiltration in the stroma
ROI6 Cancer within the duct, a few invasive carcinomas and fibrous tissue, accompanied by intraductal necrosis and scattered lymphocyte infiltration in the stroma
ROI7 Invasive carcinoma, intraductal carcinoma and fibrous tissue, accompanied by intraluminal necrosis
ROI8 A few cases of invasive cancer and necrotic tissue, with scattered lymphocyte infiltration
J
CD8A+ABCA12+TIGIT- cells distance to CD8A+ABCA12+TIGIT+ cells
K
CD8A+ABCA12+
Positive Cells (%)
Positive (n=5)
Negative (n=30)
HER2
L
CD8A+ABCA12+
Luminal A (n=15)
Luminal B (n=8)
HER2+ (n=5)
TNBC (n=9)
Subtype
M
CD8A+ABCA12+
II (n=17)
III (n=18)
Grade
N
CD8A+ABCA12+
High=11
Low=10
Overall survival
P=0.0388
Days
O
CD8A+ABCA12+
High=11
Low=10
Progression-free survival
P=0.0160
Days

1

Figure 2 In-depth characterization of the previously uncharacterized exhausted CD8A⁺ABCA12⁺ T cell subset

(A) Violin plots showing differential expression of exhaustion-related genes between CD8A⁺ABCA12⁺ and CD8A⁺ABCA12⁻ cells (*P < 0.05, ***P < 0.001, ****P < 0.0001). (B) Schematic of the flow cytometry workflow for marker expression analysis. Single-cell suspensions were isolated from breast cancer surgical specimens and analyzed by flow cytometry to compare marker expression between CD8A⁺ABCA12⁺ and CD8A⁺ABCA12⁻ cells, including exhaustion-related (C), tissue-resident memory (TRM)-associated (D), stemness-related (E), activation-related (F), proliferation-related (G), and effector-related (H) markers (*P < 0.05, **P < 0.01, ***P < 0.001, ****P < 0.0001).

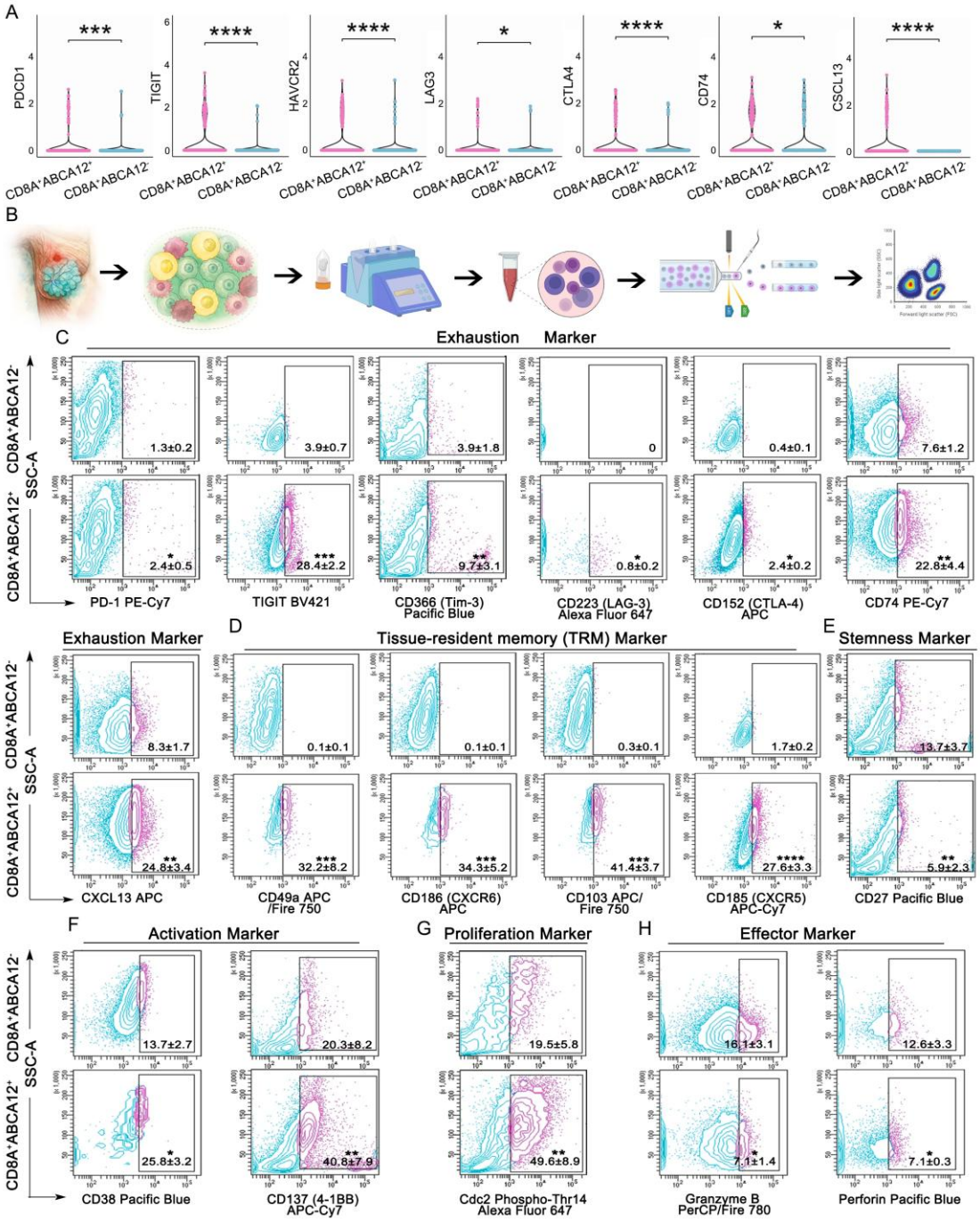


Figure 3 Tumor-initiating PROM1⁺SLC27A4⁺ cells engage in crosstalk with CD8A⁺ABCA12⁺ cells through the EGF-EGFR ligand-receptor axis

(A-D) Correlation of PROM1⁺SLC27A4⁺ cell proportion with clinicopathological features of breast cancer, including molecular subtypes (A), expression levels across PBMCs, adjacent non-tumor tissues, and tumor tissues (B), and expression in cases with or without lymph node metastasis (C) or lung metastasis (D) (***P* < 0.01, ****P* < 0.001). (E) Dot plot showing the strength of ligand-receptor interactions between PROM1⁺SLC27A4⁺ and CD8A⁺ABCA12⁺ subpopulations. (F-G) SCENIC-derived histogram (F) and heatmaps (G) depicting transcription factor STAT5 activity. (H) Protein-protein interaction (PPI) network of STAT5 target genes. (I) Western blot (WB) analysis of protein expression in the indicated cell subpopulations following the specified treatments. (J-K) qPCR and WB quantification of TIGIT (J) and ABCA12 (K) gene and protein expression in CD8A⁺ABCA12⁺ cells following co-culture with PROM1⁺SLC27A4⁺ cells and subsequent *STAT5* knockdown.

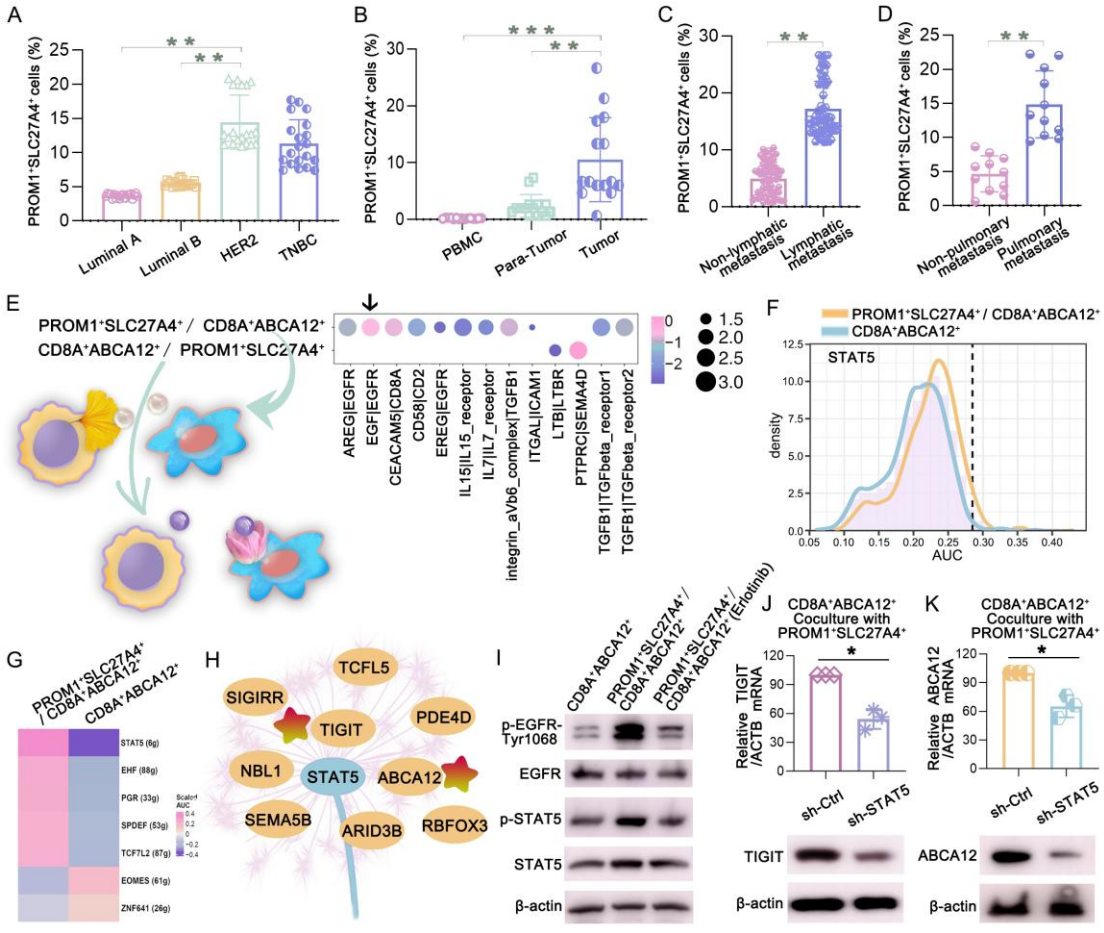


Figure 4 Spatial transcriptomic profiling of CD8A$^+$ABCA12$^+$ T cell exhaustion trajectories using stLearn trajectory and neighbor analyses

(A) Spatial localization of CD8A$^+$ABCA12$^+$, CD8A$^+$ITGAE$^+$, and PROM1$^+$SLC27A4$^+$ subpopulations across five HER2-positive breast cancer invasive carcinoma samples. (B-F) For each sample, local differentiation trajectories were associated with functional modeling based on the differentiation timing of CD8A$^+$ABCA12$^+$ and CD8A$^+$ITGAE$^+$ cells, with spatiotemporal distances computed between the CD8A$^+$ITGAE$^+$ subcluster (designated as 0) and the CD8A$^+$ABCA12$^+$ subcluster (designated as 1). (G-K) Differentiation trees depicting inter-subcluster trajectories from CD8A$^+$ITGAE$^+$ cells (indigo-outlined regions) to CD8A$^+$ABCA12$^+$ cells (ginger yellow-outlined regions) across five samples. (L) Transition genes along the CD8A$^+$ITGAE$^+$-to-CD8A$^+$ABCA12$^+$ differentiation trajectory, with upregulated genes shown in cherry pink and downregulated genes in navy blue; branches significantly enriched in exhaustion-related genes are highlighted. (M-Q) Spatial neighbor analysis based on Euclidean distance, using PROM1$^+$SLC27A4$^+$ cells as reference points. Top panels: distance heatmaps; bottom panels: density curves of CD8A$^+$ITGAE$^+$ and CD8A$^+$ABCA12$^+$ cell distribution relative to PROM1$^+$SLC27A4$^+$ reference points. (R) Spatial axis from malignant to boundary to nonmalignant regions defined using Cottrazm-based comprehensive pathology annotation. (S-T) Ridge plots comparing the regional distribution of PROM1$^+$SLC27A4$^+$ versus PROM1$^+$SLC27A4$^-$ cells (S) and CD8A$^+$ABCA12$^+$ versus CD8A$^+$ABCA12$^-$ cells (T) across nonmalignant (Normal), boundary (Bdy), and malignant (Mal) regions (*P < 0.05, **P < 0.01, ns: not significant).


A
gene_type
CD8A⁻ABCA12⁻
CD8A⁺ITGAE⁺
PROM1⁺SLC27A4⁺
B
C
D
E
F
G
Pseudoroot
H
Pseudoroot
I
Pseudoroot
J
Pseudoroot
K
Pseudoroot
L
TIGIT
Spearman correlation coefficient
M
PROM1+SLC27A4+_distance
N
PROM1+SLC27A4+_distance
O
PROM1+SLC27A4+_distance
P
PROM1+SLC27A4+_distance
Q
PROM1+SLC27A4+_distance
celltype
PROM1+SLC27A4+
CD8A+ABCA12+
CD8A+ITGAE+
density
distance to PROM1+SLC27A4+ cells
R
Type
Normal
Bdy
Mal1
Mal2
Mal3
Mal
S
Normal
Bdy
Mal
ns
*
Cell Percent (%)
PROM1+SLC27A4+
PROM1+SLC27A4-
T
Normal
Bdy
Mal
ns
*
**
Cell Percent (%)
CD8A+ABCA12+
CD8A+ABCA12-

1

Figure 5 Integrated spatial metabolomic and transcriptomic profiling reveals lignoceric acid-centered spatial gradients between PROM1⁺SLC27A4⁺ and CD8A⁺ABCA12⁺ enriched regions

(A, Ⅰ-Ⅴ) Integrated spatial metabolomic and transcriptomic analysis across five samples, employing a random line-drawing strategy with six sampling points per sample. (B, Ⅰ-Ⅴ) Each tissue section was partitioned into 16 zones centered on the tissue midpoint, with corresponding spatial mapping diagrams generated for each zone. (C, Ⅰ-Ⅴ) Spot-level assignment based on CD8A⁺ABCA12⁺ and PROM1⁺SLC27A4⁺ transcriptomic signature scores. As spatial transcriptomic data were not resolved at single-cell resolution, spots were assigned according to relative expression scores of the CD8A⁺ABCA12⁺ and PROM1⁺SLC27A4⁺ gene programs. (D, Ⅰ-Ⅴ) Spatial intensity distribution maps of lignoceric acid- and ceramide-related metabolites constructed across spatial radiation zones. (E, Ⅰ-Ⅴ) Enrichment and gradient distribution of specific metabolites in CD8A⁺ABCA12⁺ and PROM1⁺SLC27A4⁺ cell-dense regions.

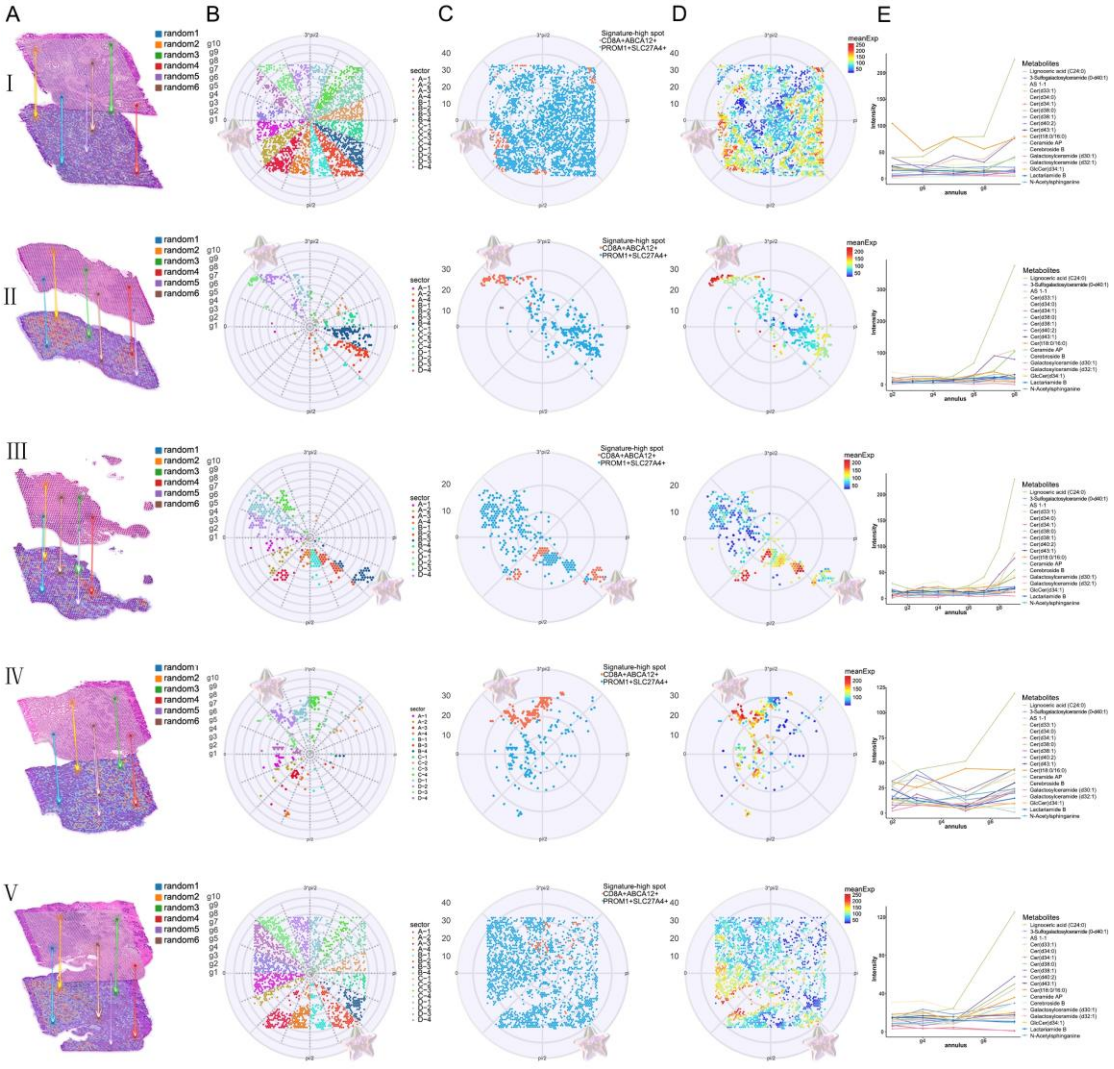


Figure 6 $CD8A^+ABCA12^+$ T cells promote peridroplet mitochondrial remodeling in $PROM1^+SLC27A4^+$ tumor cells via ABCA12-dependent lignoceric acid transfer

(A) Schematic of lipid droplet tracing in $CD8A^+ABCA12^+$-$PROM1^+SLC27A4^+$ co-cultures using Red C12-labeled fatty acids. (B) Schematic overview of the experimental design. (C) Confocal microscopy images showing lipid droplet distribution under indicated treatment conditions. Scale bar = 10 μm. (D) Transmission electron microscopy (TEM) images illustrating mitochondrial morphology and lipid droplet distribution under indicated treatment conditions. Scale bar = 0.5 μm. (E) qPCR quantification of MFN2 expression under two treatment conditions (**$P < 0.01$). (F-G) Mitochondrial fusion efficiency (F) and PDM abundance (G) following MFN2 knockout under the indicated culture conditions (**$P < 0.01$). (H) Live-cell confocal microscopy images showing mitochondrial and lipid droplet distribution under indicated culture conditions. Scale bar = 5 μm. (I) Mitochondrial ATP synthesis rates under indicated culture conditions (**$P < 0.01$). (J) Schematic illustrating PDM-mediated lipid droplet transfer into mitochondria to promote ATP synthesis. (K) Schematic of the integrated workflow for subcellular 3D reconstruction using ZEISS electron microscopy, the ZEISS arivis Cloud platform, and ZEISS arivis Pro software. (L) Representative 2D and 3D TEM images of $PROM1^+SLC27A4^+$ cells cultured alone (1st-2nd panels, scale bar = 5 μm) or co-cultured with $CD8A^+ABCA12^+$ cells (3rd-4th panels, scale bar = 5 μm for 2D, 2 μm for 3D). In 2D images, mitochondria are pseudocolored magenta and nuclei sky blue; in 3D images, mitochondria are pseudocolored cyan and nuclei ginger yellow. (M) 3D reconstructed panoramic and locally magnified TEM images of $PROM1^+SLC27A4^+$ cells cultured alone (left) or co-cultured with $CD8A^+ABCA12^+$ cells (right). Scale bar = 1 μm (panoramic views). Mitochondria are pseudocolored ginger yellow, lipid droplets orange, and nuclei dark blue. (N) Ridge plots comparing mitochondrial sphericity, volume, mitochondria-to-nucleus distance, and mitochondria-to-lipid droplet distance between $PROM1^+SLC27A4^+$ cells cultured alone and co-cultured with $CD8A^+ABCA12^+$ cells (***$P < 0.001$). (O) Ridge plots comparing lipid droplet sphericity, volume, lipid droplet-to-nucleus distance, and lipid droplet-to-mitochondria distance between the same two conditions (*$P < 0.05$).

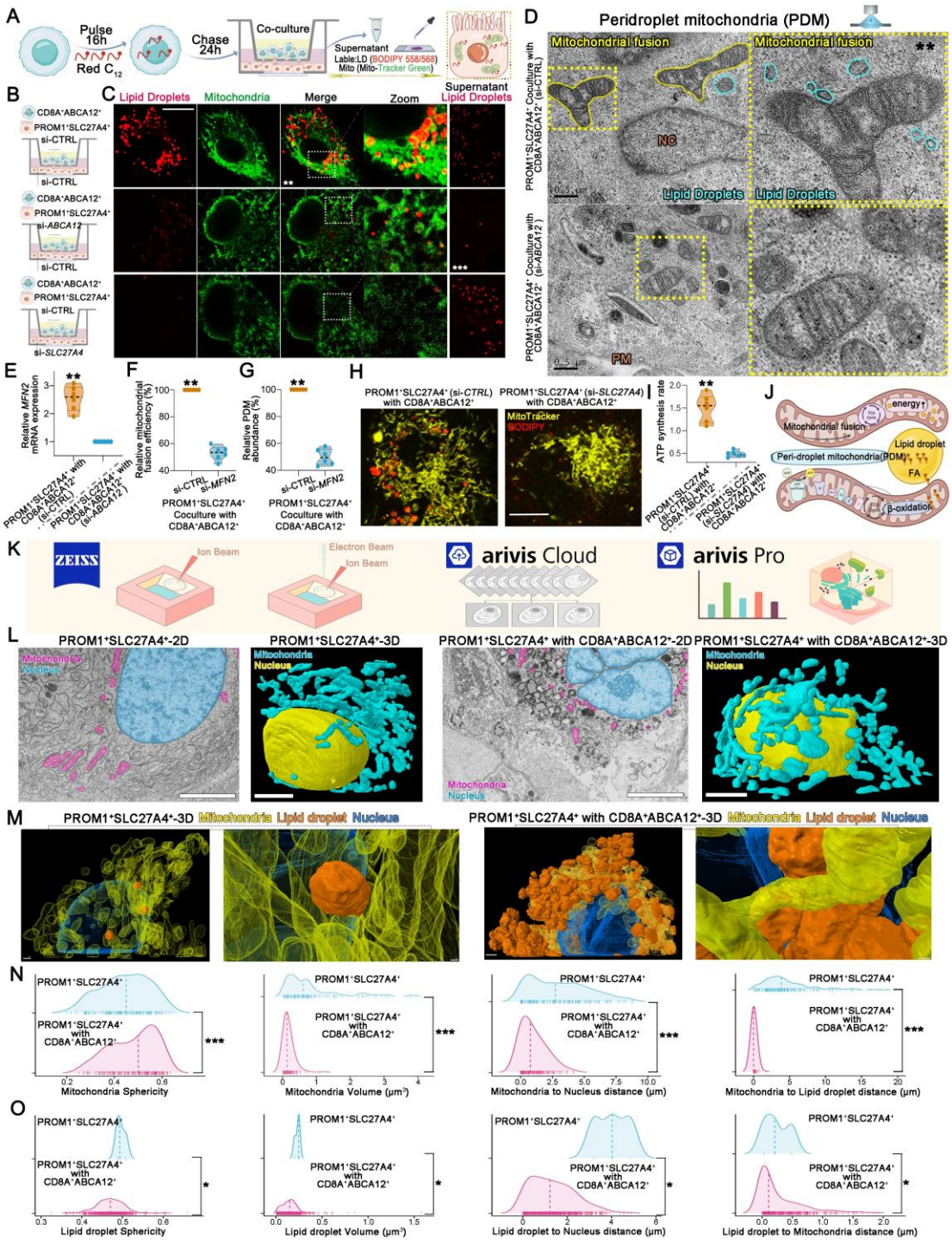
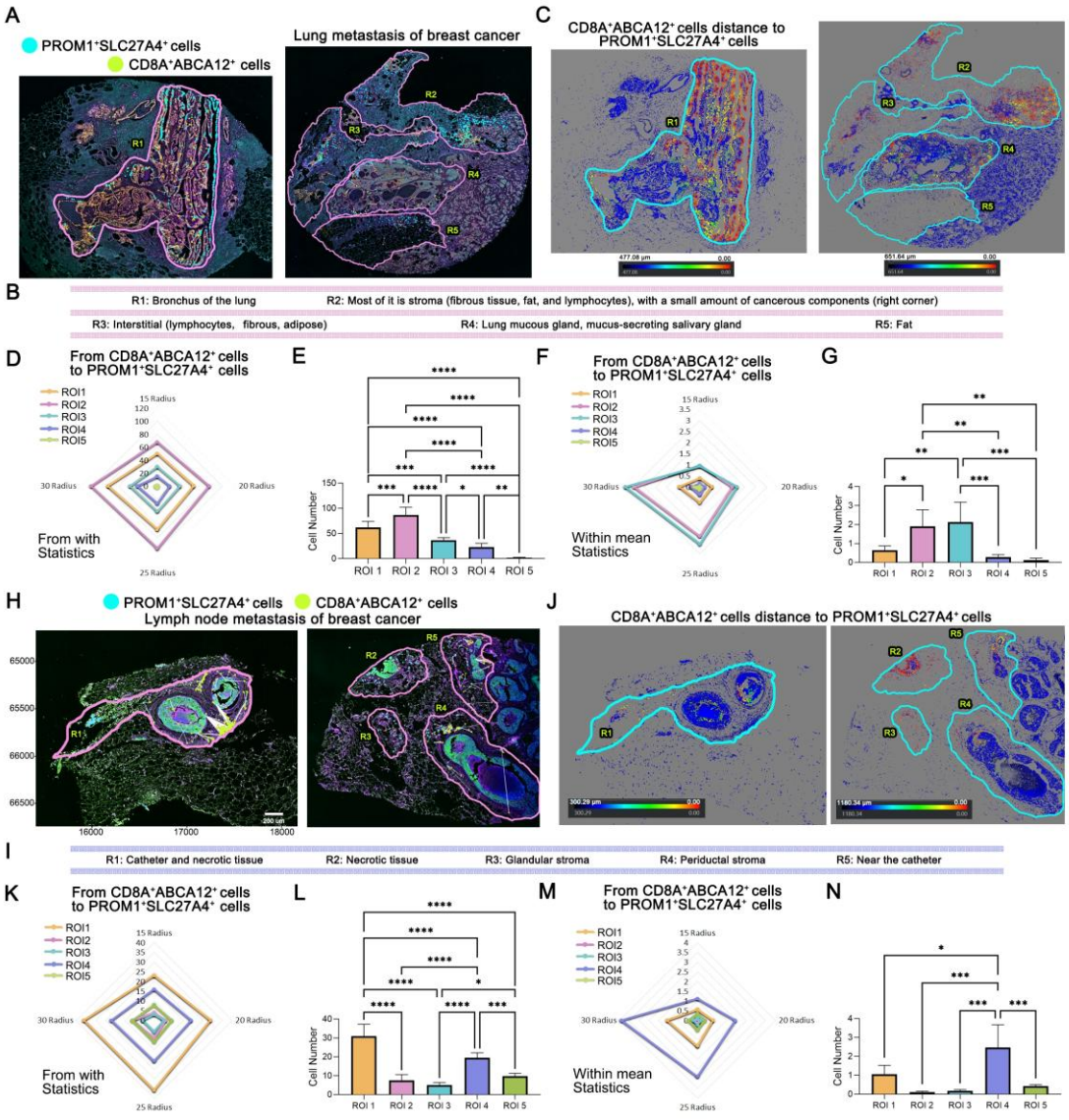

A
Pulse 16h
Red C12
Chase 24h
Co-culture
Supernatant
Lable:LD (BODIPY 558/568)
Mito (Mito-Tracker Green)
Supernatant Lipid Droplets
B
CD8A+ABCA12+
PROM1+SLC27A4+
si-CTRL
si-ABCA12
si-SLC27A4
C
Lipid Droplets
Mitochondria
Merge
Zoom
Supernatant Lipid Droplets
D
Peridroplet mitochondria (PDM)
Mitochondrial fusion
NG
Lipid Droplets
PM
PROM1+SLC27A4+ Coculture with CD8A+ABCA12+ (si-CTRL)
PROM1+SLC27A4+ Coculture with CD8A+ABCA12+ (si-ABCA12+)
E
Relative MFN2 mRNA expression
F
Relative mitochondrial fusion efficiency (%)
si-CTRL
si-MFN2
PROM1+SLC27A4+ Coculture with CD8A+ABCA12+
G
Relative PDM abundance (%)
H
PROM1+SLC27A4+ (si-CTRL) with CD8A+ABCA12+
PROM1+SLC27A4+ (si-SLC27A4) with CD8A+ABCA12+
MitoTracker
BODIPY
ATP synthesis rate
J
energy↑
Mitochondrial fusion
Peri-droplet mitochondria(PDM)
Lipid droplet
FA
β-oxidation
K
ZEISS
Ion Beam
Electron Beam
arivis Cloud
arivis Pro
L
PROM1+SLC27A4+-2D
PROM1+SLC27A4+-3D
PROM1+SLC27A4+ with CD8A+ABCA12+-2D
PROM1+SLC27A4+ with CD8A+ABCA12+-3D
Mitochondria
Nucleus
M
PROM1+SLC27A4+-3D Mitochondria Lipid droplet Nucleus
PROM1+SLC27A4+ with CD8A+ABCA12+-3D Mitochondria Lipid droplet Nucleus
N
PROM1+SLC27A4+
PROM1+SLC27A4+ with CD8A+ABCA12+
Mitochondria Sphericity
Mitochondria Volume (μm³)
Mitochondria to Nucleus distance (μm)
Mitochondria to Lipid droplet distance (μm)
O
Lipid droplet Sphericity
Lipid droplet Volume (μm³)
Lipid droplet to Nucleus distance (μm)
Lipid droplet to Mitochondria distance (μm)

Figure 7 Spatial distribution characteristics of $CD8A^+ABCA12^+$ and $PROM1^+SLC27A4^+$ subsets in breast cancer patients with lung or lymph node metastasis

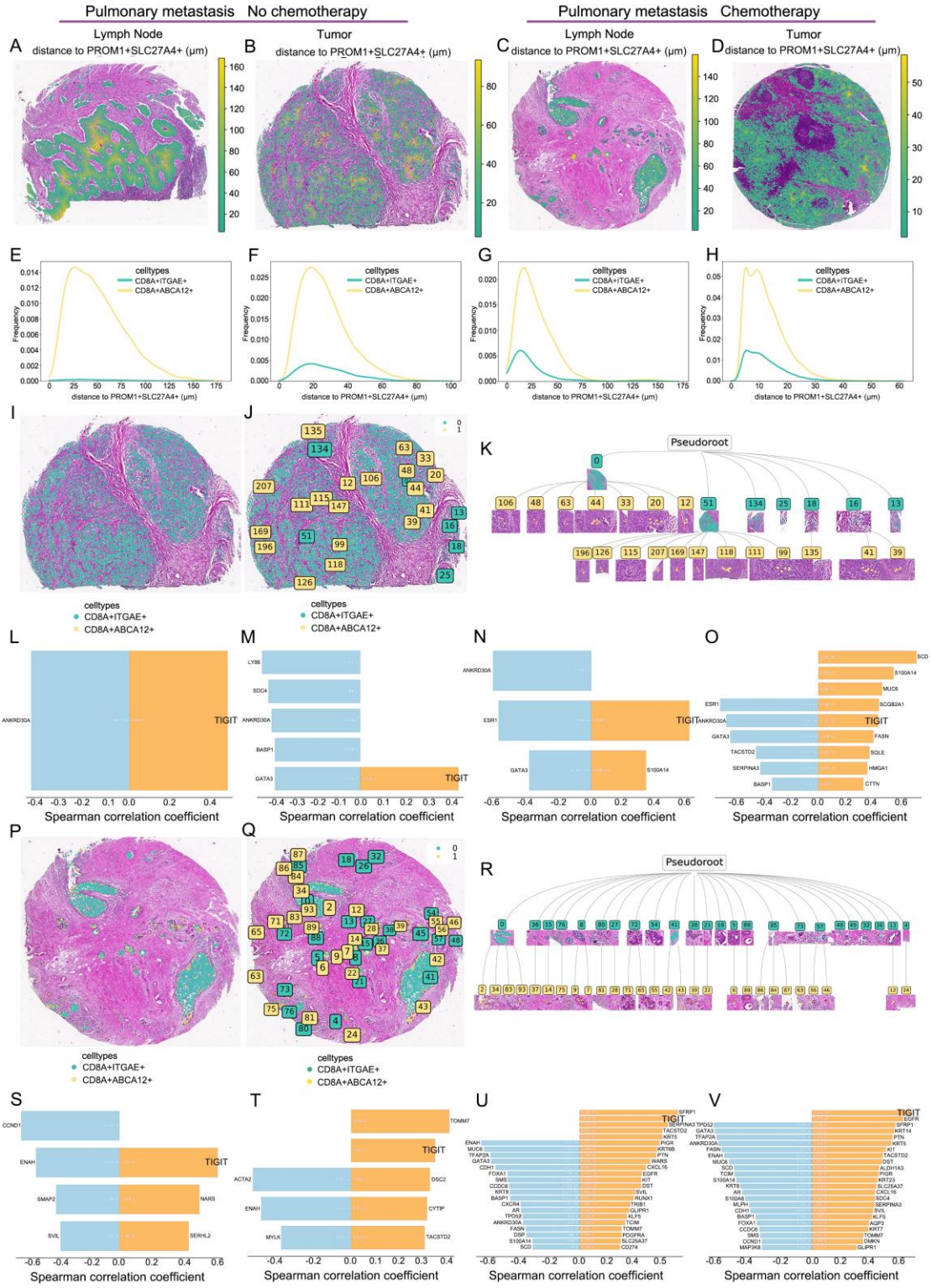
(A) PhenoptrReports-based identification of the nearest $PROM1^+SLC27A4^+$ cell to each $CD8A^+ABCA12^+$ cell across multiple regions of interest (ROIs), integrated into a panoramic view of breast cancer lung metastasis pathological sections. (B) Overview of pathological features in five key regions. (C) Distance-based spatial heatmaps of $PROM1^+SLC27A4^+$ and $CD8A^+ABCA12^+$ cells. Scale ranges: 0-477.08 μm (left panel), 0-651.64 μm (right panel). (D-G) Spatial geographic maps characterizing the spatial scale between the two subsets using "From with" (D) and "Within mean" (F) metrics, with corresponding quantitative statistics (E, G) (*P < 0.05, **P < 0.01, ***P < 0.001, ****P < 0.0001). (H) PhenoptrReports-based identification of the nearest $PROM1^+SLC27A4^+$ cell to each $CD8A^+ABCA12^+$ cell across multiple ROIs in breast cancer lymph node metastasis pathological sections, stitched into a panoramic image. (I) Summary of pathological characteristics in five major regions. (J) Distance-based spatial heatmaps of $PROM1^+SLC27A4^+$ and $CD8A^+ABCA12^+$ cells. Scale ranges: 0-300.29 μm (left panel), 0-1180.34 μm (right panel). (K-N) Spatial geographic maps characterizing the spatial scale between the two subsets using "From with" (K) and "Within mean" (M) metrics, with corresponding quantitative statistics (L, N) (*P < 0.05, ***P < 0.001, ****P < 0.0001).


A
PROM1⁺SLC27A4⁺ cells
CD8A⁺ABCA12⁺ cells
Lung metastasis of breast cancer
R1
R2
R3
R4
R5
C
CD8A⁺ABCA12⁺ cells distance to PROM1⁺SLC27A4⁺ cells
B
R1: Bronchus of the lung
R2: Most of it is stroma (fibrous tissue, fat, and lymphocytes), with a small amount of cancerous components (right corner)
R3: Interstitial (lymphocytes, fibrous, adipose)
R4: Lung mucous gland, mucus-secreting salivary gland
R5: Fat
D
From CD8A⁺ABCA12⁺ cells to PROM1⁺SLC27A4⁺ cells
ROI1
ROI2
ROI3
ROI4
ROI5
15 Radius
20 Radius
25 Radius
30 Radius
From with Statistics
E
Cell Number
ROI 1
ROI 2
ROI 3
ROI 4
ROI 5
F
From CD8A⁺ABCA12⁺ cells to PROM1⁺SLC27A4⁺ cells
Within mean Statistics
G
Cell Number
H
PROM1⁺SLC27A4⁺ cells
CD8A⁺ABCA12⁺ cells
Lymph node metastasis of breast cancer
J
CD8A⁺ABCA12⁺ cells distance to PROM1⁺SLC27A4⁺ cells
I
R1: Catheter and necrotic tissue
R2: Necrotic tissue
R3: Glandular stroma
R4: Periductal stroma
R5: Near the catheter
K
From CD8A⁺ABCA12⁺ cells to PROM1⁺SLC27A4⁺ cells
From with Statistics
L
Cell Number
M
From CD8A⁺ABCA12⁺ cells to PROM1⁺SLC27A4⁺ cells
Within mean Statistics
N
Cell Number

1

Figure 8 Spatial *in situ* analysis of breast tumor metastasis and chemoresistance linked to the exhaustion gradient of CD8A$^+$ABCA12$^+$ subpopulations

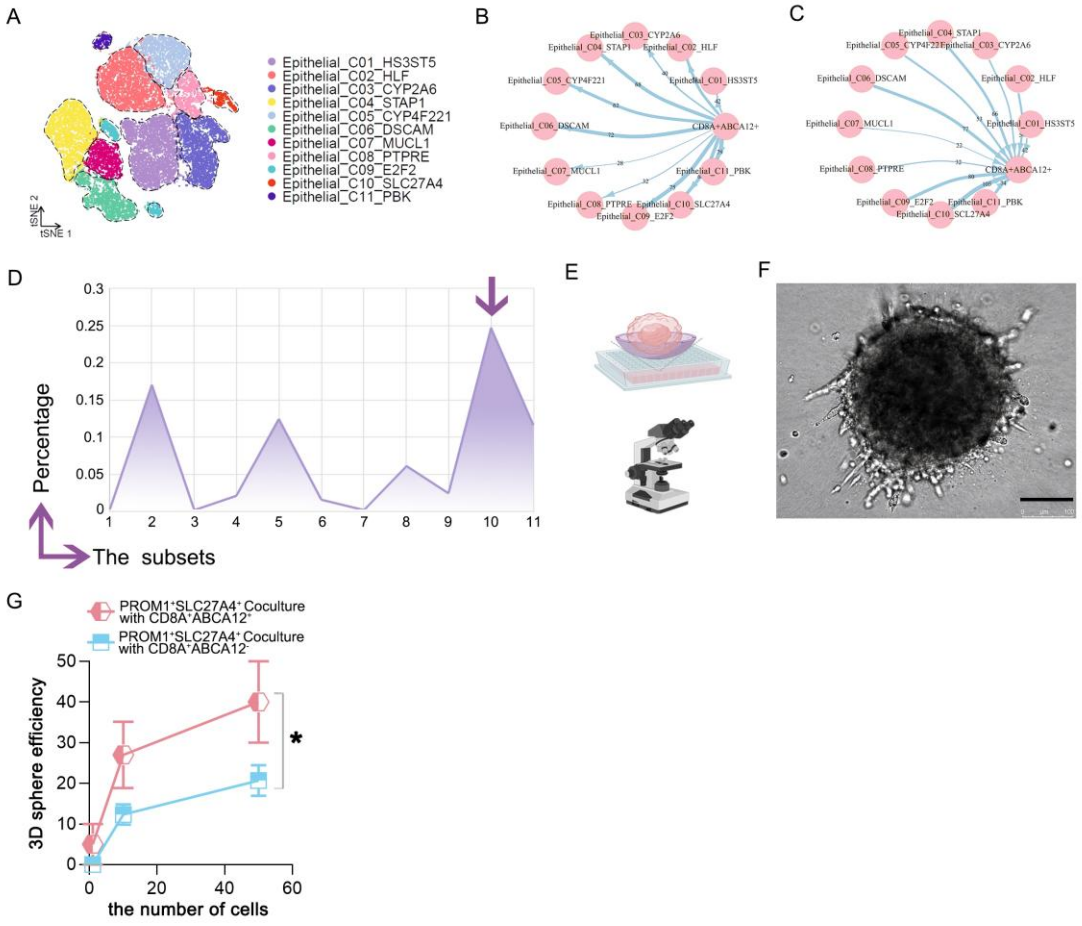
(A-B) Spatial in situ detection of embolic cancer cell clusters in lymph nodes (A) and matched primary breast tumors (B) from a chemotherapy-naive HER2-positive breast cancer patient with distant lung metastasis. (C-D) Corresponding spatial in situ detection of embolic cancer cell clusters in lymph nodes (C) and matched primary breast tumors (D) from chemotherapy-treated HER2-positive breast cancer patients with distant lung metastasis. (E-H) Euclidean distance-based spatial neighbor analysis using PROM1$^+$SLC27A4$^+$ cells as reference points. Heatmaps show distance magnitude from CD8A$^+$ABCA12$^+$ and CD8A$^+$ITGAE$^+$ cells to PROM1$^+$SLC27A4$^+$ reference points, with corresponding density curves plotted for matched samples. (I, P) Spatial in situ detection of CD8A$^+$ITGAE$^+$ and CD8A$^+$ABCA12$^+$ subpopulations in primary breast tumors from chemotherapy-naive (I) or chemotherapy-treated (P) HER2-positive breast cancer patients with distant lung metastasis. (J, Q) Local differentiation trajectories associated with functional modeling based on differentiation timing, with spatiotemporal distances calculated between the CD8A$^+$ITGAE$^+$ subcluster (early differentiation, designated as 0) and the CD8A$^+$ABCA12$^+$ subcluster (late differentiation, designated as 1). (K, R) Differentiation trees illustrating inter-subcluster differentiation paths from CD8A$^+$ITGAE$^+$ to CD8A$^+$ABCA12$^+$ according to differentiation order. (L-O, S-V) Transition genes along the CD8A$^+$ITGAE$^+$-to-CD8A$^+$ABCA12$^+$ differentiation trajectory, with upregulated genes shown in vintage yellow and downregulated genes in vintage blue.


Pulmonary metastasis No chemotherapy
Pulmonary metastasis Chemotherapy
A
Lymph Node
distance to PROM1+SLC27A4+ (μm)
B
Tumor
distance to PROM1+SLC27A4+ (μm)
C
Lymph Node
distance to PROM1+SLC27A4+ (μm)
D
Tumor
distance to PROM1+SLC27A4+ (μm)
E
F
G
H
celltypes
CD8A+ITGAE+
CD8A+ABCA12+
Frequency
distance to PROM1+SLC27A4+ (μm)
I
J
celltypes
CD8A+ITGAE+
CD8A+ABCA12+
K
Pseudoroot
L
M
N
O
TIGIT
Spearman correlation coefficient
P
Q
celltypes
CD8A+ITGAE+
CD8A+ABCA12+
R
Pseudoroot
S
T
U
V
TIGIT
Spearman correlation coefficient

1

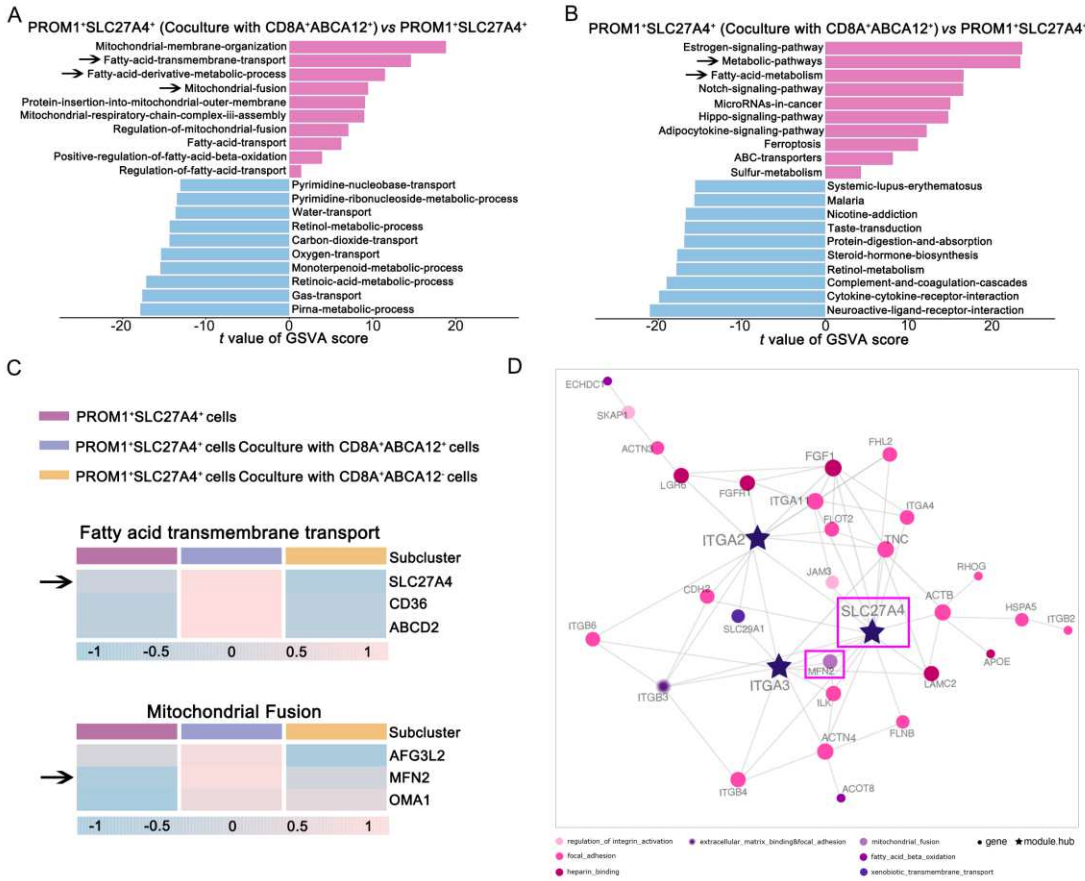
SFigure 1 Supplementary to Figure 1

(A) Epithelial cells were identified using EPCAM, KRT19, and PROM1 markers and further subdivided into 11 distinct subsets. (B-C) Cell communication networks depicting outgoing (B) and incoming (C) signals between the 11 epithelial cell subpopulations and $CD8A^{+}ABCA12^{+}$ cells. (D) Ridge plot showing the proportion of the $PROM1^{+}SLC27A4^{+}$ subpopulation across the 11 epithelial cell subsets. (E) Schematic of the 3D spheroid formation workflow in ultra-low attachment culture plates and differential interference contrast (DIC) microscopy observation. (F) DIC microscopy images of 3D spheroid formation. Scale bar = 100 μm. (G) Quantification of spheroid counts across groups (*P < 0.05).



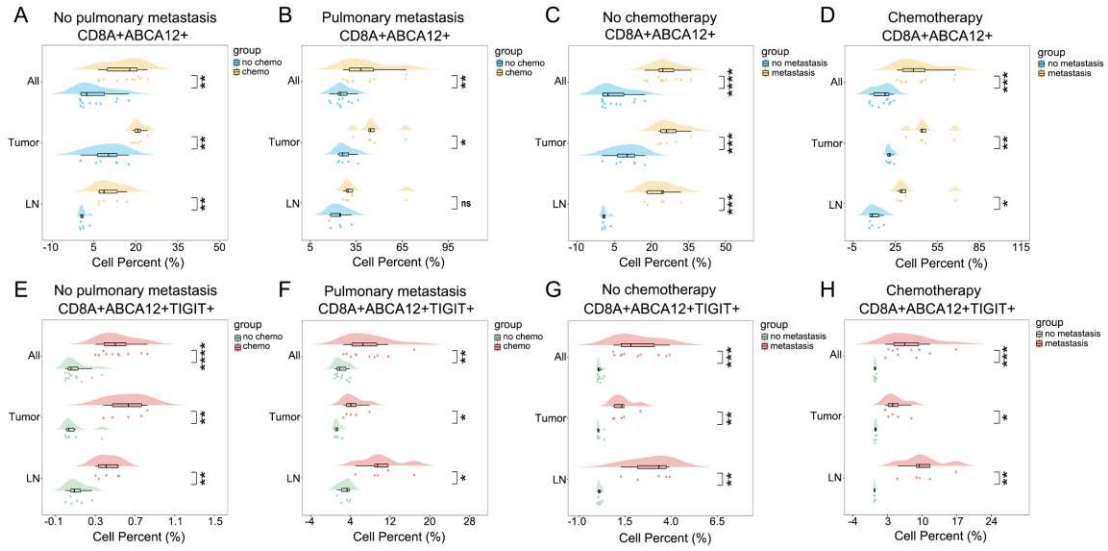
SFigure 2 Supplementary to Figure 6

(A-B) Gene Set Variation Analysis (GSVA) identifying differences in Gene Ontology (GO) enrichment (A) and Kyoto Encyclopedia of Genes and Genomes (KEGG) pathways (B) between PROM1⁺SLC27A4⁺ cells co-cultured with CD8A⁺ABCA12⁺ cells and PROM1⁺SLC27A4⁺ cells cultured alone. (C) Heatmap showing expression of genes associated with key biological functions in the indicated subpopulations. (D) Gene co-expression network modules in PROM1⁺SLC27A4⁺ cells co-cultured with CD8A⁺ABCA12⁺ cells, generated using the MEGENA package. Node size reflects gene significance and color denotes pathway enrichment.



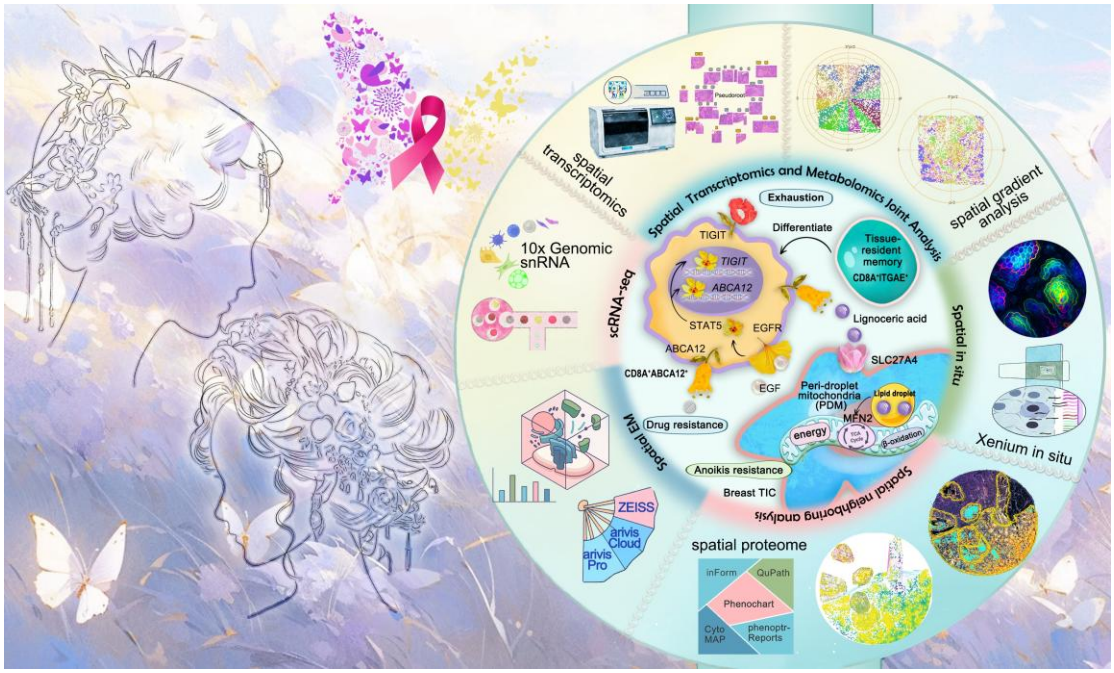
SFigure 3 Supplementary to Figure 8

(A-B) Raincloud plots showing $CD8A^+ABCA12^+$ subpopulation expression in cancer embolic niches of $HER2^+$ breast cancer patients without (A) or with (B) distant lung metastasis, comparing paired primary breast tumor and lymph node regions, and differences between chemotherapy-treated and chemotherapy-naive groups. (C-D) Raincloud plots showing $CD8A^+ABCA12^+$ subpopulation expression in cancer embolic niches of chemotherapy-naive (C) or chemotherapy-treated (D) $HER2^+$ breast cancer patients, comparing paired primary breast tumor and lymph node regions, and differences between patients with and without distant lung metastasis. (E-F) Raincloud plots showing $CD8A^+ABCA12^+TIGIT^+$ subpopulation expression in cancer embolic niches of $HER2^+$ breast cancer patients without (E) or with (F) distant lung metastasis, comparing paired primary breast tumor and lymph node regions, and differences between chemotherapy-treated and chemotherapy-naive groups. (G-H) Raincloud plots showing $CD8A^+ABCA12^+TIGIT^+$ subpopulation expression in cancer embolic niches of chemotherapy-naive (G) or chemotherapy-treated (H) $HER2^+$ breast cancer patients, comparing paired primary breast tumor and lymph node regions, and differences between patients with and without distant lung metastasis. $*P < 0.05$, $**P < 0.01$, $***P < 0.001$, $****P < 0.0001$, N.S.: no significant difference.



SFigure 4 Graphical Abstract

Left Panel: As the adage goes, "When you gaze long into an abyss, the abyss also gazes into you"—cancer cells may have long targeted immune cells, "eavesdropping" on the mechanisms that induce their exhaustion and hijacking exhausted T cells to support their own survival and metastasis. This adversarial relationship is visualized through sketch-style figures. The background features an idyllic pastoral scene with fluttering butterflies, symbolizing the aspiration for rebirth and recovery. Upper Middle Panel: A breast cancer-iconic motif inlaid with a butterfly—its left wing intact and right wing incomplete—epitomizes the challenges encountered in breast cancer treatment. Right Peripheral Panels: Integrated multi-omics approaches establishing a systematic strategy to address core research questions. Central Right Panel: Key molecular mechanisms elucidated in this study.



Supplementary Files

This is a list of supplementary files associated with this preprint. Click to download.

- 3.CD8STable1.docx
- 3.CD8STable1.docx
- 3.CD8STable1.docx
- CD8SFig.2.tif
- CD8SFig.2.tif
- CD8SFig.2.tif
- CD8SFig.4.jpg
- CD8SFig.4.jpg
- CD8SFig.4.jpg
- CD8SFig.3.tif
- CD8SFig.3.tif
- CD8SFig.3.tif
- CD8SFig.1.jpg
- CD8SFig.1.jpg
- CD8SFig.1.jpg